UC Santa Cruz

UC Santa Cruz Previously Published Works

Title

Orbital forcing of the Paleocene and Eocene carbon cycle

Permalink

Journal

ISSN

Authors

Zeebe, Richard E
Westerhold, Thomas
Littler, Kate
et al.

Publication Date

DOI

Peer reviewed

RESEARCH ARTICLE

Key Points:
- We present the first estimates of orbital-scale variations in atmospheric CO_2 during the late Paleocene and early Eocene
- High-latitude mechanisms are unlikely drivers of orbitally paced changes in the late Paleocene-early Eocene
- We also reveal a mechanism for the large δ^{13}C-eccentricity lag at the 400 kyr period observed in Paleocene, Oligocene, and Miocene sections

Supporting Information:
- Supporting Information S1

Correspondence to:
R. E. Zeebe,
zeebe@soest.hawaii.edu

Orbital forcing of the Paleocene and Eocene carbon cycle

Richard E. Zeebe[1] [iD], Thomas Westerhold[2] [iD], Kate Littler[3], and James C. Zachos[4] [iD]

[1]School of Ocean and Earth Science and Technology, University of Hawai'i at Mānoa, Honolulu, Hawaii, USA, [2]MARUM, University of Bremen, Bremen, Germany, [3]Camborne School of Mines, University of Exeter, Penryn, UK, [4]Earth and Planetary Sciences Department, University of California, Santa Cruz, California, USA

Abstract Multimillion-year proxy records across the Paleocene and Eocene show prominent variations on orbital time scales. The cycles, which have been identified at various sites across the globe, preferentially concentrate spectral power at eccentricity and precessional frequencies. It is evident that these cycles are an expression of changes in global climate and carbon cycling paced by astronomical forcing. However, little is currently known about the link between orbital forcing and the carbon cycle-climate system and the amplitude of associated atmospheric CO_2 variations. Here we use simple and complex carbon cycle models to explore the basic effect of different orbital forcing schemes and noise on the carbon cycle. Our primary modeling target is the high-resolution, ~7.7 Myr long, benthic isotope record at Ocean Drilling Program Site 1262 in the South Atlantic. For direct insolation forcing (as opposed to artificial eccentricity-tilt-precession), one major challenge is understanding how the system transfers spectral power from high to low frequencies. We discuss feasible solutions, including insolation transformations analogous to electronic AC-DC conversion (DC'ing). Regarding mechanisms, we focus on tropical insolation and a long-term carbon imbalance in terrestrial organic burial/oxidation but do not rule out other scenarios. Our analysis shows that high-latitude mechanisms are unlikely drivers of orbitally paced changes in the late Paleocene-early Eocene (LPEE) Earth system. Furthermore, we provide constraints on the origin and isotopic composition of a possible LPEE cyclic carbon imbalance/source responding to astronomical forcing. Our simulations also reveal a mechanism for the large δ^{13}C-eccentricity lag at the 400 kyr period observed in Paleocene, Oligocene, and Miocene sections. We present the first estimates of orbital-scale variations in atmospheric CO_2 during the late Paleocene and early Eocene.

1. Introduction

Recent progress in developing long, high-fidelity proxy records from Paleocene-Eocene marine and continental sedimentary sequences has revealed cyclic variations at frequencies corresponding to the main beats of astronomical forcing [*Curry et al.*, 1995; *Röhl et al.*, 2000; *Cramer et al.*, 2003; *Lourens et al.*, 2005; *Westerhold et al.*, 2007; *Zachos et al.*, 2010; *Galeotti et al.*, 2010; *Littler et al.*, 2014; *Lauretano et al.*, 2016; *Abels et al.*, 2016]. Hence, it is evident that orbital variations have paced oscillations in Paleocene and Eocene (P/E) climate and carbon cycling, including several of the more transient events, or hyperthermals. However, the dynamics behind the observed Milanković cycles during the early Paleogene are largely unknown; comprehensive modeling studies to elucidate the link between astronomical forcing and P/E climate-carbon cycle processes are so far missing. In fact, very few carbon cycle modeling studies have tackled the problem at all, regardless of age (for Oligocene, Miocene, and Plio-Pleistocene, see *Pälike et al.* [2006b], *Ma et al.* [2011], and *Russon et al.* [2010]). Simple isotopic mass balance models have been employed [*Cramer et al.*, 2003; *Laurin et al.*, 2015]. However, these models were not designed as prognostic tools to compute changes in carbon cycle variables such as ocean carbon inventory, calcite compensation depth (CCD), and atmospheric CO_2.

In addition, a prominent, but poorly understood, feature of P/E records and their spectra is the concentration of power at eccentricity frequencies (e.g., Figure 1), while insolation forcing is dominated by climatic precession (Figure 4). (Below we simply use "precession" for climatic precession [cf. *Laskar et al.*, 2004].) The Earth system must directly respond to the full insolation forcing and the various frequencies carried by this signal. Artificial forcing functions composed of pure eccentricity-tilt-precession (ETP) components are useful conceptually [e.g., *Imbrie et al.*, 1984] but do not represent the actual forcing. Thus, in reality, mechanism(s) must
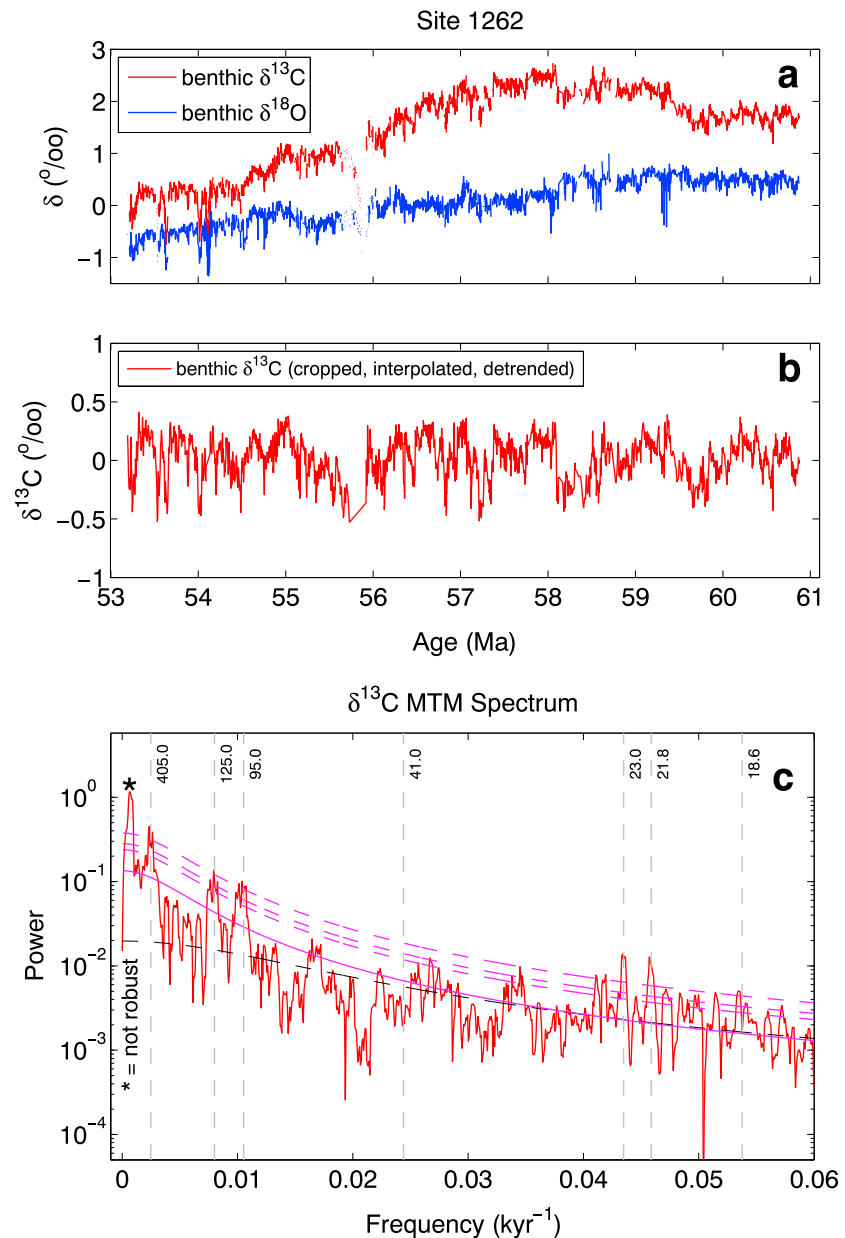
Figure 1. Benthic isotope records from ODP Site 1262 [*Littler et al.*, 2014]. (a) Raw data, age model after *Westerhold et al.* [2015]. (b) Cropped, linear interpolated, and detrended $\delta^{13}C$ time series; PETM and ELMO removed. (c) MTM spectrum of Figure 1b with $K = 3$ tapers ($K = 2p - 1$, where $p = 2$ is the time-bandwidth product). Vertical dashed lines indicate periods (kyr). Note that the position of the highest peak around 1.6 Myr (labeled asterisk) depends on the detrending choice and is hence not robust (see section 6.3). Purple lines (AR(1) red noise fit) [*Meyers*, 2012, 2014; *Patterson et al.*, 2014] and black line [*Mann and Lees*, 1996; *Ghil et al.*, 2002] may aid in visually identifying significant peaks.

be active that transfer power from precession to eccentricity frequencies [e.g., *Short et al.*, 1991; *Ripepe and Fischer*, 1991; *Huybers and Wunsch*, 2003]. In the present paper, we explore three main questions related to astronomical forcing and the response of the early Paleogene Earth system. (1) What are viable links between orbital forcing and the P/E carbon cycle and climate system? (2) What are possible mechanisms that concentrate spectral power at eccentricity frequencies? (3) How did atmospheric CO_2 vary (magnitude and phase) with respect to the orbital cycles documented in P/E proxy records?

The paper is organized as follows. We start by defining our modeling target. Then we propose a forcing mechanism based on tropical insolation changes and test how insolation modifications (e.g., operations similar to electronic AC-DC conversion) and noise affect the results of a minimal carbon cycle model.

Next, we apply a simple forcing to a more complex carbon cycle model (LOSCAR) to highlight the basic response of, and leads and lags between, different carbon cycle variables. (LOSCAR stands for Long-term Ocean-atmosphere-Sediment CArbon cycle Reservoir model [*Zeebe*, 2012, 2013b]). Finally, we apply the full insolation forcing to LOSCAR and present the first estimates of variations in atmospheric CO_2 associated with orbital cycles during the Paleocene and Eocene.

2. Modeling Target and Time Series Analysis

Our primary modeling target for the present study is the astronomically tuned, high-resolution ($\Delta t \simeq 3.3$ kyr) benthic isotope record at Ocean Drilling Program (ODP) Site 1262 in the South Atlantic, ~60.9–53.2 Ma [*Littler et al.*, 2014; *Westerhold et al.*, 2015] (Figure 1a). The site's paleowater depth and paleolatitude at the P/E boundary were approximately 3600 m and 40°S [*Zachos et al.*, 2005, http://www.paleolatitude.org]. The record consists of ~2300 paired carbon and oxygen isotope values of benthic foraminifera (*Nuttallides truempyi*), representing an ~7.7 Myr long deep-ocean record across the late Paleocene and early Eocene. For resolving global signals, benthic records are preferable given that bottom water properties, e.g., temperature and δ^{13}C, are time averaged, so there is minimal local seasonality bias.

For time series analysis, the PETM (Paleocene-Eocene Thermal Maximum) and ELMO were removed from the long-term benthic record (Figure 1b). These events are distinct from orbital-scale variations (see section 5.2) and may bias the analysis of the long-term cyclicity in the record, which is of interest here. We note, however, that including or excluding the hyperthermals has little effect on the spectrum, except for the 405 kyr cycle (see supporting information). The record was detrended (by removing piecewise linear trends for every 15% of the record), cropped (detrended δ^{13}C values outside [−0.6, 0.4] removed), and linearly resampled at $\Delta t \simeq$ 3.5 kyr ($N = 2167$ for δ^{13}C). For the resulting 7.7 Myr time series the highest and lowest (Nyquist and Rayleigh) frequencies are hence $f_N = 1/(2\Delta t) = 0.14$ kyr^{-1} and $f_R = 1/(N\Delta t) = 0.13$ Myr^{-1}, corresponding to periods ($\mathcal{T}$) of 7 kyr and 7.7 Myr. The power spectrum of the time series was computed using the multitaper method (MTM) with $K = 3$ tapers, where $K = 2p - 1$ and $p = 2$ is the time-bandwidth product [*Thomson*, 1982; *Percival and Walden*, 1993; *Mann and Lees*, 1996; *Ghil et al.*, 2002]. Data, model output, and time series analyses were performed using MATLAB routines developed during this project. For full δ^{13}C and δ^{18}O spectra up to Nyquist frequency (including the half-precession band), see supporting information.

Estimates of minimum errors in single-frequency lines corresponding to peaks in the MTM spectrum were obtained using Monte Carlo simulations [e.g., *Muller and MacDonald*, 2002], yielding a standard deviation $\sigma_f \simeq 0.15 \times f_R = 2 \times 10^{-5}$ kyr^{-1} (Appendix A). On the other hand, the frequency resolution at which two lines can be separated is given by the MTM resolution bandwidth, $\rho_f = p \cdot f_R = 2f_R = 2.6 \times 10^{-4}$ kyr^{-1} (Appendix A). Given these uncertainty estimates and the fact that the age model is based on astronomical tuning of the long (405 kyr) and short (~100 kyr) eccentricity cycles [*Westerhold et al.*, 2008] suggests that the MTM spectrum and assignment for $\mathcal{T} \lesssim 400$ kyr ($f \gtrsim 0.0025$ kyr^{-1}, Figure 1c). However, this is not the case for periods on million-year time scale. First, while the estimated error in frequency space is constant, it grows with the period because $\mathcal{T} = 1/f$ (at 2.4 Myr, $2\sigma_\mathcal{T} \simeq 225$ kyr, $\rho_\mathcal{T} \simeq 1.5$ Myr). Second, and more importantly, the amplitude and position of, for instance, the lowest-frequency peak depends on (rather arbitrary) detrending details. For example, taking larger blocks of the record for piecewise linear detrending retains longer periods, which enlarges and shifts the peak toward lower f (Figure 1c). Such frequency assignments are hence not robust (for a less problematic approach, see section 6.3).

3. Tropical Insolation Forcing

Spectral analyses of various long-term records across the Paleocene and early Eocene show very little or no power in the obliquity band [*Westerhold et al.*, 2007; *Zachos et al.*, 2010; *Westerhold and Röhl*, 2013; *Littler et al.*, 2014; *Meyers*, 2015]; see section 6.3 for more details. Hence, we propose a low-latitude (tropical) forcing mechanism that links variations in tropical insolation to changes in Earth's carbon cycle on orbital time scale, most likely indirectly through effects on precipitation patterns (see section 3.1). Note that we do not rule out potential effects of obliquity forcing on low-latitude climate [*Bosmans et al.*, 2015]. However, if this mechanism was significant during the Paleocene and early Eocene, one would expect a notable obliquity signal, which is not the case in deep-sea isotope records. Also, given that precession-induced changes in low-latitude climate phenomena such as monsoon systems appear much larger than from obliquity [*Bosmans et al.*, 2014], the latter component might be undetectable. Thus, we focus on low-latitude forcing.
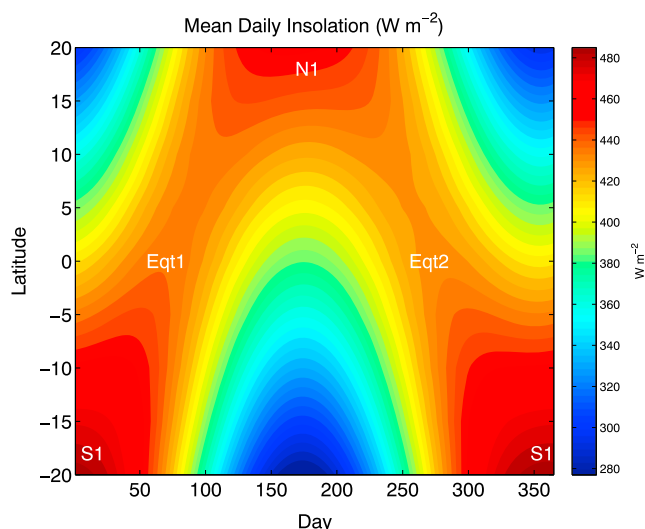
Figure 2. Present mean daily insolation (MATLAB routine from Eisenman and Huybers, eisenman.ucsd.edu/code.html). N1 and S1: single annual maximum during boreal and austral summer. Eqt1 and Eqt2: double annual insolation maxima on the equator as the Sun crosses overhead twice a year around spring and fall equinoxes.

At latitudes $\gtrsim 20°$N/S, the present mean daily tropical insolation shows the usual single annual maximum during boreal and austral summer (labels N1 and S1, Figure 2). In addition, at the equator two annual insolation maxima are observed as the Sun crosses the equator overhead twice a year around the spring and fall equinoxes (labels Eqt1 and Eqt2, Figure 2). Possible effects of the equatorial double insolation peaks on climate have been discussed previously [*Short et al.*, 1991; *Crowley et al.*, 1992; *Park et al.*, 1993; *Berger et al.*, 2006; *Ashkenazy and Gildor*, 2008]. We propose that both the single off-equator insolation maxima ($\gtrsim 20°$N/S) and the equatorial double peaks can trigger changes in the burial of terrestrial organic carbon (C_{org}) when insolation exceeds a certain threshold (see below for a discussion of mechanisms). Here we use "C_{org} burial" synonymously with a net imbalance in organic oxidation and burial (indistinguishable). As an illustration of the tropical insolation forcing over time, consider the mean daily insolation at 20°N/S during Northern Hemisphere (NH) and Southern Hemisphere (SH) summer solstice over the past 500 kyr (N1 and S1, Figure 3), as well as the mean daily equatorial insolation during the spring and fall equinoxes (Eqt1 and Eqt2, Figure 3). These four insolation quantities (I_1, I_2, I_3, and I_4 in the following) are dominated by precession and hence amplitude modulated by eccentricity (e), which is the envelope of precession. We propose that each of the I_i can force changes in carbon cycling (when above the long-term mean), and thus, we construct a normalized insolation forcing ($\mathcal{I}$) based on a superposition (weighted average) of the I_i.

First, from the I_i we create demeaned ($\bar{I}_i$) and "clipped" insolation time series (if $\bar{I}_i < 0$, set $\bar{I}_i = 0$). This transformation is similar to electronic AC-DC conversion, in the following referred to as "DC'ing" (aka rectification), which reflects the assumption that insolation above average will cause a carbon cycle response on orbital time scales. Using different weights $0 \leq w_i \leq 1$ (to be varied), we will test individual forcing contributions and combinations (flavors) of the I_i by using weighted averages (w_i's assumed stationary):

$$I = \sum_{i=1}^{4} w_i \bar{I}_i. \qquad (1)$$

Finally, we normalize the forcing

$$\mathcal{I}_0 = (I - \bar{I}) / \max |I - \bar{I}| . \qquad (2)$$

Below, we also use $\mathcal{I} = 1 + \alpha \mathcal{I}_0$ as the normalized insolation forcing, where α encodes the sign and strength of the forcing.

We have studied the effect of various superpositions of the tropical insolation curves on $\mathcal{I}$ by varying the weights w_i, effectively producing a blend of clipped and DC'd forcing (Figures 3c–3e). For example, the flavor $\boldsymbol{w} = [0\ 0\ 1\ 1]$ represents a forcing composed of the equatorial double insolation maxima at the equinoxes (Figure 3c), which includes the possibility of generating a half-precession cycle (~11 kyr) in Earth's climate system and carbon cycle [*Berger et al.*, 2006; *Ashkenazy and Gildor*, 2008]. Furthermore, $\boldsymbol{w} = [1\ 1\ 1\ 1]$ is a simple
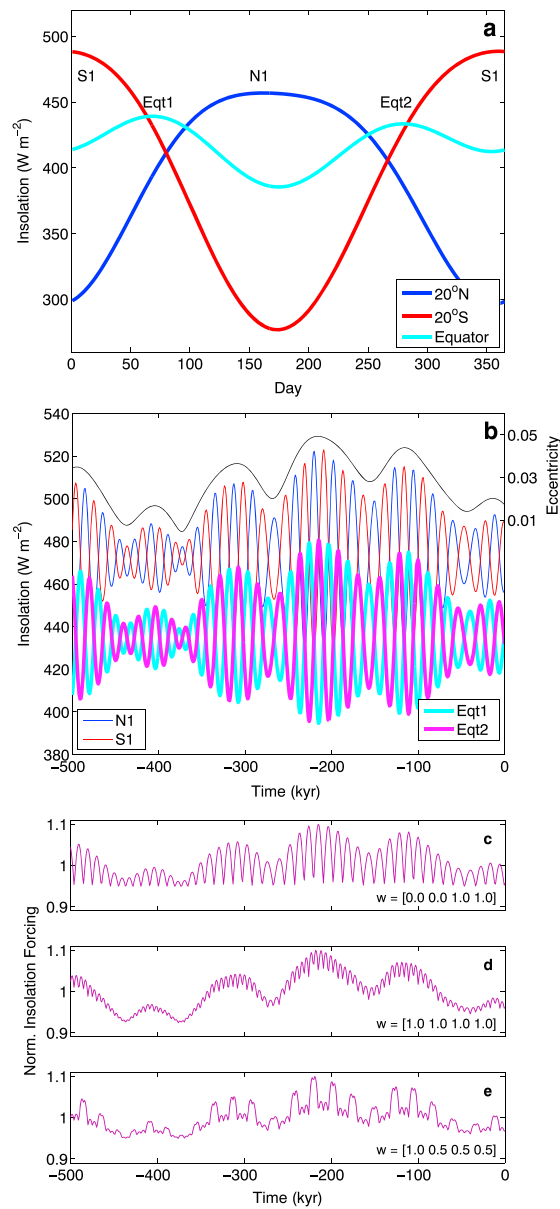
Figure 3. Insolation and constructed forcing. (a) Present mean daily insolation; maxima are labeled N1, S1, Eqt1, and Eqt2. (b) Eccentricity and mean daily insolation at 20°N/S during Northern Hemisphere and Southern Hemisphere summer solstice over the past 500 kyr (N1 and S1) and on the equator during the spring and fall equinoxes (Eqt1 and Eqt2). (c) Example of normalized forcing with different N1, S1, Eqt1, and Eqt2 components or flavor w = [N1 S1 Eqt1 Eqt2] = [0 0 1 1] (see text). (d) w = [1 1 1 1]. (e) w_d = [1 0.5 0.5 0.5] (default).

linear superposition of all four insolation curves with equal weights (Figure 3d), while $w_d = [1\ 0.5\ 0.5\ 0.5]$, for instance, reflects a possible asymmetry in the tropical forcing efficacy between the two hemispheres and assigns less weight to the equatorial double peaks (Figure 3e). The latter flavor provides a good fit to the target spectrum (see below), including the half-precession band (Figures S1 and S3), and will be taken as the default forcing.

3.1. A Forcing Mechanism
In terms of mechanisms, the default flavor w_d would be consistent with, for instance, causes related to asymmetric land-sea distribution and asymmetric seasonal land-sea temperature contrasts in the two hemispheres [e.g., *Short et al.*, 1991]. In general, eccentricity maxima result in large precession/insolation amplitudes (Figure 3b), likely corresponding to more intense wet and dry seasons. Eccentricity minima result in small

precession/insolation amplitudes and likely more equable climates, which, we suggest, favors enhanced long-term organic carbon burial. As a result, the exogenic carbon reservoir would become isotopically heavier during eccentricity minima (recorded by δ^{13}C proxies) and lighter during eccentricity maxima. This eccentricity-δ^{13}C relationship is consistent with the phasing underpinning the construction of P/E time scales [*Cramer et al.*, 2003; *Zachos et al.*, 2010; *Littler et al.*, 2014; *Lauretano et al.*, 2016].

Analogies between P/E and modern climate phenomena such as the monsoon system are limited because of different continental configuration, baseline climate, etc. Moreover, the global climate and carbon cycle response during, e.g., the late Pleistocene (as expressed in δ^{13}C and δ^{18}O records) fundamentally differs from that of the early Paleogene, for one due to the presence/absence of large ice sheets [e.g., *Wang et al.*, 2010; *Russon et al.*, 2010; *Kirtland Turner*, 2014]. Nevertheless, late Pleistocene monsoon records indicate a direct relationship between the eccentricity-modulated precession/insolation amplitude and Asian monsoon variation on precessional time scale. For example, Chinese cave records indicate that the longest interval of reduced amplitude in Asian monsoon cycles (~20 kyr periodicity) during the past 650 kyr occurred between ~450 and ~350 kyr B.P. (including Marine Isotope Stage 11) [*Cheng et al.*, 2016], the time interval of lowest orbital eccentricity during the late Pleistocene. These records hence suggest more intense wet seasons and droughts [*Verschuren et al.*, 2009] across several precession cycles, corresponding to high eccentricity periods on ~100 kyr time scale [*Cheng et al.*, 2016], and conversely less intense wet/dry seasons during low eccentricity. We propose a loosely related mechanism for the early Paleogene with enhanced long-term average C_{org} burial occurring during low eccentricity intervals.
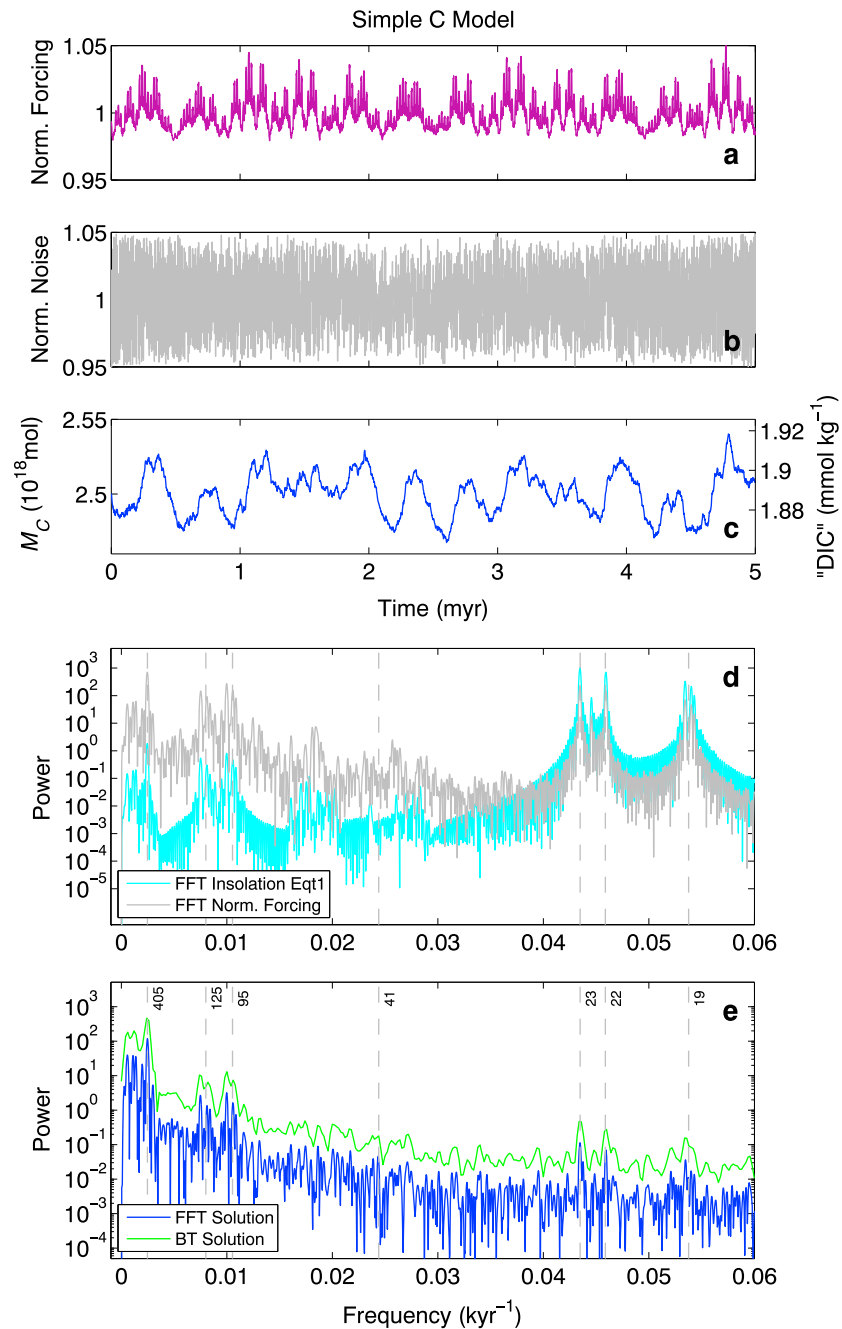
4. Forcing a Minimal Carbon Cycle Model

We first consider a simple (probably minimal) carbon cycle model, which nevertheless shows the basic system response to insolation forcing and noise. Consider a single carbon reservoir and changes due to one source and one sink:

$$\frac{dM_C}{dt} = F \cdot \mathcal{I} \cdot \mathcal{N} - \lambda M_C, \qquad (3)$$

where M_C is the carbon inventory (in mol), F is a constant influx (mol C yr^{-1}), and λ (yr^{-1}) is a sink/decay constant. The exact value picked for F is not critical, chosen here to yield a reasonable mean steady state ($F = \lambda \cdot \overline{M_C}$) on the order of observed values. We set $F = 25 \times 10^{12}$ mol yr^{-1}, $\overline{M_C} = 2.5 \times 10^{18}$ mol (30,000 Pg C), yielding $\lambda^{-1} = 100$ kyr. If the carbon inventory M_C represented the ocean only, then M_C per unit mass would be the average DIC (Dissolved Inorganic Carbon concentration, ~2 mmol kg^{-1}); cf. DIC in LOSCAR's model boxes (section 5). $\mathcal{I}$ and $\mathcal{N}$ represent normalized insolation forcing and normalized white noise with time averages $\overline{\mathcal{I}} = \overline{\mathcal{N}} = 1$. When forced with noise only, the model turns white noise into red noise, where smaller λ values (i.e., larger time constant $\tau = \lambda^{-1}$) enhance power in the lower frequencies (red spectrum). We characterize the white noise input by its maximum amplitude β ($-\beta \leq \mathcal{N} - 1 \leq \beta$). Also, a noise "correlation time" (η_c) needs to be specified, i.e., the time after which the random process changes in the numerical integration. Ideally, a truly random signal (white noise) has $\eta_c = 0$, but in practice, η_c is finite and should be chosen smaller than the fastest dynamics of the system. For orbital forcing of the simple model, we take the half-precession cycle (~11 kyr) as the fastest process and use $\eta_c \simeq 1$ kyr. We also tested $\eta_c \simeq 3$ kyr, similar to the resolution of the isotope record at Site 1262, which made little difference (for the simple model as well as for LOSCAR, section 5.2).

Applying the normalized tropical forcing $\mathcal{I} = 1 + \alpha \mathcal{I}_0$ and noise to the simple model with $\alpha = 0.05$, flavor $\boldsymbol{w}_d = [1\ 0.5\ 0.5\ 0.5]$ (see above), and noise amplitude $\beta = 0.05$, the evolution of the model's carbon inventory over, say, 5 Myr and the corresponding power spectrum are readily computed numerically (Figure 4). Insolation quantities for this experiment are from the astronomical solution La2004 [*Laskar et al.*, 2004] for the period $t = [-60, -55]$ Ma. While more recent solutions are available [*Laskar et al.*, 2011], it is important to note that all solutions are uncertain beyond ~50 Ma in the past (except for a rather stable 405 kyr eccentricity component). Fortunately, none of this is critical for the current experiment, which examines the fundamental carbon cycle response to insolation forcing and its frequency spectrum, not absolute ages. In fact, results are very similar using La2004 insolation for $t = [-60, -55]$, $[-55, -50]$, and $[-5, 0]$ Ma.

The power spectrum of the simple model's C inventory (Figure 4) shows several features similar to those of the benthic δ^{13}C spectrum at Site 1262 (Figure 1). Power at eccentricity and precessional frequencies rises above the background noise, and as expected, power in the obliquity band is practically absent. Compared

Figure 4. Forcing, output, and spectra of the minimal carbon cycle model. (a) Normalized insolation forcing (default w_d over 5 Myr). (b) Normalized noise. (c) Model solution for carbon inventory M_C (2.5×10^{18} mol C = 30,000 Pg C). If M_C was for ocean only, then "DIC" would be approximately mean ocean DIC. (d) Power spectra of insolation and normalized forcing using MATLAB's FFT (Fast Fourier Transform, "periodogram"). Vertical dashed lines indicate periods (kyr). (e) Power spectrum of model solution for M_C shown in Figure 4c. BT = Blackman-Tukey with 1/2 lags.

to the observations, the model's long eccentricity cycle (405 kyr) is more pronounced relative to the short eccentricity cycle (95, 125 kyr). Overall, the model's spectrum is also slightly "more red" than the 1262 benthic δ^{13}C spectrum; i.e., the model has a stronger tendency to concentrate power toward the lower frequencies (Figure 4). Full spectra up to Nyquist frequency (including the half-precession band) are shown in the supporting information.

Importantly, however, the model and data response at precessional frequencies is strongly muted compared to the forcing. For instance, the 23 and 125 kyr components have nearly equal power in the normalized
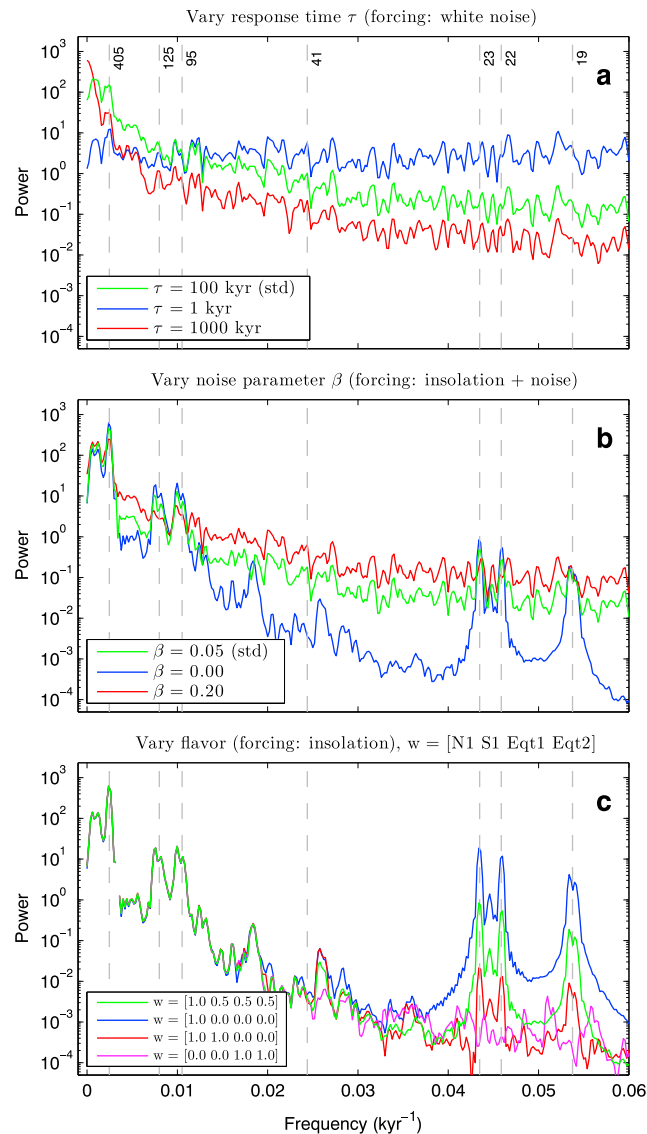
Figure 5. Spectral response of the minimal carbon cycle model (M_C) to parameter variation from 5 Myr runs. All spectra based on Blackman-Tukey with 1/2 lags. (a) Response time τ; std = standard value, (b) noise, and (c) insolation forcing flavor, **w** = [N1 S1 Eqt1 Eqt2] (see text). Vertical dashed lines indicate periods (kyr).

forcing (Figure 4d). However, the power in the model response at 23 kyr is almost 30 times smaller than at 125 kyr (Figure 4e; peak heights and integrated power give similar numbers). This effect is predominantly due to the model's decay constant λ or time constant $\tau = \lambda^{-1}$ (= 100 kyr in the standard setup). In contrast, using $\tau = 1$ kyr (see also Figure 5a), the 125/23 kyr power ratio in the model's response is near unity (the noise background has very little effect on this ratio). Thus, the carbon cycle's long time constant is responsible for reducing precessional power in the system response relative to the forcing [cf. *Pälike et al.*, 2006b]. This effect is different from "shifting" power in the forcing itself from precession to eccentricity (see DC'ing above).

4.1. Varying Parameters and Forcing Flavors

As mentioned above, for white noise forcing, larger values of the time constant $\tau = \lambda^{-1}$ enhance power in the lower frequencies and reduce power at higher frequencies (red spectrum), whereas a small τ (rapid response time) produces white noise. These features are well captured by the minimal carbon cycle model, run over 5 Myr (Figure 5a). Forcing of the simple model with normalized insolation and strong noise ($\beta = 0.2$) essentially masks all significant peaks at precessional and eccentricity frequencies, except below ~1/405 kyr^{-1}

(Figure 5b). Without noise ($\beta = 0$), the insolation forcing also produces a red background spectrum (due to the response time effect, standard $\tau = 100$ kyr) but in this case large peaks in the spectrum of the model's carbon inventory prominently rise above the background at all significant forcing frequencies (Figure 5b).

Different forcing flavors (weights for [N1 S1 Eqt1 Eqt2] insolation contributions) mostly affect the model spectrum in the precession band (Figure 5c). For example, applying only 20°N insolation forcing ($\boldsymbol{w} = [1\ 0\ 0\ 0]$) produces strong precession peaks in the model response, which is expected because 20°N insolation (as well as the clipped time series) is dominated by precession (Figure 3b). In contrast, applying only equatorial insolation forcing with equal weights ($\boldsymbol{w} = [0\ 0\ 1\ 1]$) produces no significant precession peaks because the forcing is dominated by the half-precession cycle (Figures 3c and S4). In summary, the spectrum of the simple model's response is consistent with observations (Figure 1c), when a certain combination of response time, noise, and forcing flavor is used. A response time on the order of 100 kyr (approximately residence time of carbon) generates the necessary "redness" of the spectrum, while the right balance between noise amplitude and forcing flavor ensures that the precession peaks rise above the background noise.

5. Forcing the LOSCAR Carbon Cycle Model
5.1. LOSCAR's Response to Simple Sinusoidal Forcing
To illustrate the response of different carbon cycle components to periodic forcing at different frequencies, we first apply a simple sinusoidal forcing to LOSCAR with periods $\mathcal{T} = 23$, 100, and 400 kyr (Figures 6 and 7). (The corresponding forcing term in equation (3) would be a sinusoidal $F \cdot \mathcal{I}$.) This exercise is only to analyze the basic model response to a simple forcing; for LOSCAR's response to actual insolation forcing and comparison with the target data, see section 5.2. In the model, we force the carbon flux due to organic carbon burial (F_{gb}) with a δ^{13}C value of -23‰:

$$F_{gb} = F_{gb}^0 \left[1 - \gamma \sin(\omega t)\right], \tag{4}$$

where superscript "0" refers to the initial steady state flux, $\gamma = 0.3$, $\omega = 2\pi f = 2\pi/\mathcal{T}$, and f is the forcing frequency. The negative sign in the forcing term ensures that eccentricity/insolation maxima correspond to δ^{13}C minima in the exogenic carbon pool (see above). LOSCAR's response to the 400 kyr forcing turned out to be most instructive as it shows the largest leads and lags between components and forcing (Figure 6). At all frequencies, model DIC (dissolved inorganic carbon), pCO$_2$, and δ^{13}C lag the forcing to varying degrees, with lags increasing with the forcing period (Figure 7; DIC, δ^{13}C, and [CO$_3^{2-}$] shown are for the deep Atlantic and deep Pacific box). The notable exception is [CO$_3^{2-}$] at 400 kyr (see below).

As C_{org} burial declines, carbon accumulates in the ocean-atmosphere system and DIC rises (Figure 6). Yet DIC keeps rising beyond the time of minimum burial, as F_{gb} is still below its steady state value F_{gb}^0 and carbon keeps accumulating. Only when C_{org} burial rises above F_{gb}^0, DIC starts dropping. This is a typical accumulation effect, where DIC largely represents the integral over the forcing. In fact, if we take the forcing as $\sin(\omega t)$, then the integral is $-\cos(\omega t)/\omega$ and the phase angle between the two functions is $\pi/2$ or lag $\mathcal{T}/4$. Thus, we would expect DIC to lag the forcing by roughly $\mathcal{T}/4$, i.e., [5.8 25 100] kyr at $\mathcal{T} = [23\ 100\ 400]$ kyr. The corresponding LOSCAR simulations give [7.5 29 101] kyr.

The lag of pCO$_2$ relative to the forcing is somewhat smaller than for DIC because pCO$_2$ is also a function of total alkalinity (TA, not shown), which rises in parallel to DIC, while CaCO$_3$ burial in deep-sea sediments is reduced as the CCD shoals (Figure 6). The whole-ocean TA increase stabilizes the saturation state and initiates the reversal toward more alkaline conditions (reduces acidification), which causes pCO$_2$ to reach its maximum before DIC does. The carbon isotope ratio of DIC (δ^{13}C) consistently leads DIC by thousands of years (up to $\sim$40 kyr at the 400 kyr forcing, Appendix B). Briefly, the reason is that total C and ^{13}C have different long-term response times. In a simplified view, the ocean's chemistry largely controls the total C response, while the carbon residence time controls the ^{13}C response (see Appendix B).

Strikingly, deep-sea [CO$_3^{2-}$] and the CCD *lead* the forcing under 400 kyr sinusoidal forcing. The reason for this seemingly infeasible behavior is the feedback between atmospheric CO$_2$ and weathering. The mechanism is similar to that causing the pCO$_2$-DIC lead (described above) but is amplified via enhanced weathering. In LOSCAR, carbonate and silicate weathering fluxes (F_{cc} and F_{si}) are calculated as

$$F_{\mathrm{cc}} = F_{\mathrm{cc}}^0 \left(p\mathrm{CO}_2 / p\mathrm{CO}_2^0\right)^{n_{\mathrm{cc}}} \tag{5}$$

$$F_{\mathrm{si}} = F_{\mathrm{si}}^0 \left(p\mathrm{CO}_2 / p\mathrm{CO}_2^0\right)^{n_{\mathrm{si}}} \tag{6}$$
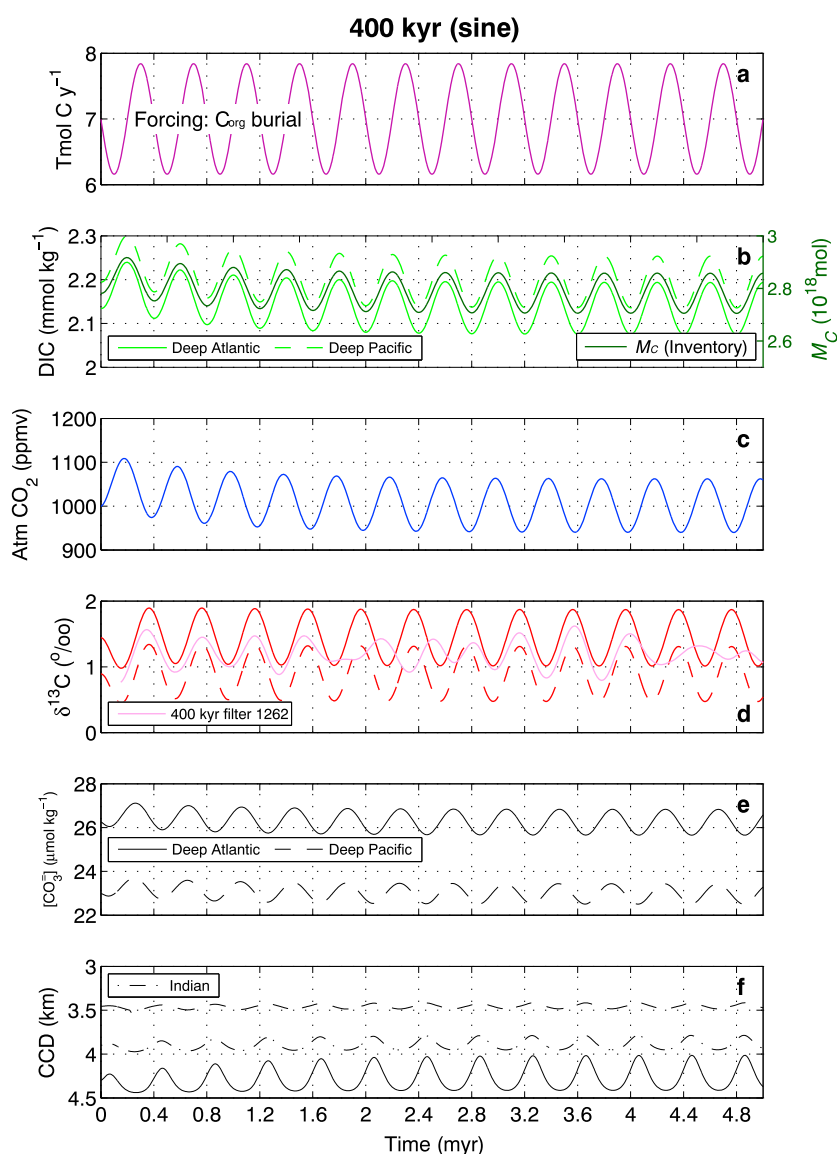
Figure 6. LOSCAR's response to sinusoidal 400 kyr forcing. (a) Prescribed forcing: C_{org} burial (7 Tmol C yr^{-1} = 0.084 Pg C yr^{-1}). (b) Dissolved inorganic carbon (DIC) and ocean DIC inventory (M_C). (c) Atmospheric CO$_2$. (d) Red lines: model $\delta^{13}C_{DIC}$. Light purple line: sixth-order Butterworth 400 kyr filter ($\pm30\%$ cutoff) of the 1262 benthic δ^{13}C record [*Littler et al.*, 2014; *Westerhold et al.*, 2015] with arbitrary amplitude and offset. (e) Deep [CO$_3^{2-}$]. (f) CCD.

where the superscript 0 refers to the initial (steady state) value of the weathering flux and pCO$_2$, respectively. The parameters n_{cc} and n_{si} control the strength of the weathering feedback [*Uchikawa and Zeebe*, 2008; *Zeebe*, 2012]. As pCO$_2$ rises in response to the forcing (Figure 6), weathering fluxes increase (equations (5) and (6)), causing a more rapid rise in TA, which speeds up the stabilization of the saturation state. As a result, the [CO$_3^{2-}$] minimum occurs before the C_{org}-burial minimum in the forcing for the 400 kyr sinusoid (phase angle $\varphi < 0$). Note that *Russon et al.* [2010] defined phase angles differently (all $\varphi > 0$). However, in their Figure 4, for instance, the pCO$_2$ minimum occurs before the forcing minimum, corresponding to $\varphi < 0$ here.

Additional runs (not shown) confirmed that the [CO$_3^{2-}$]-DIC lead strongly depends on the parameters n_{cc} and n_{si}. A stronger weathering feedback causes the lead to increase; for $n_{cc} = n_{si} = 0$ (constant weathering), [CO$_3^{2-}$] actually lags the forcing. Thus, in some cases the model-computed phase relationships depend strongly on model setup and parameters; they can also be changed by applying additional forcing (section 5.3.1). Nevertheless, our results for the [CO$_3^{2-}$] and CCD phase direction provides an explanation for the surprising
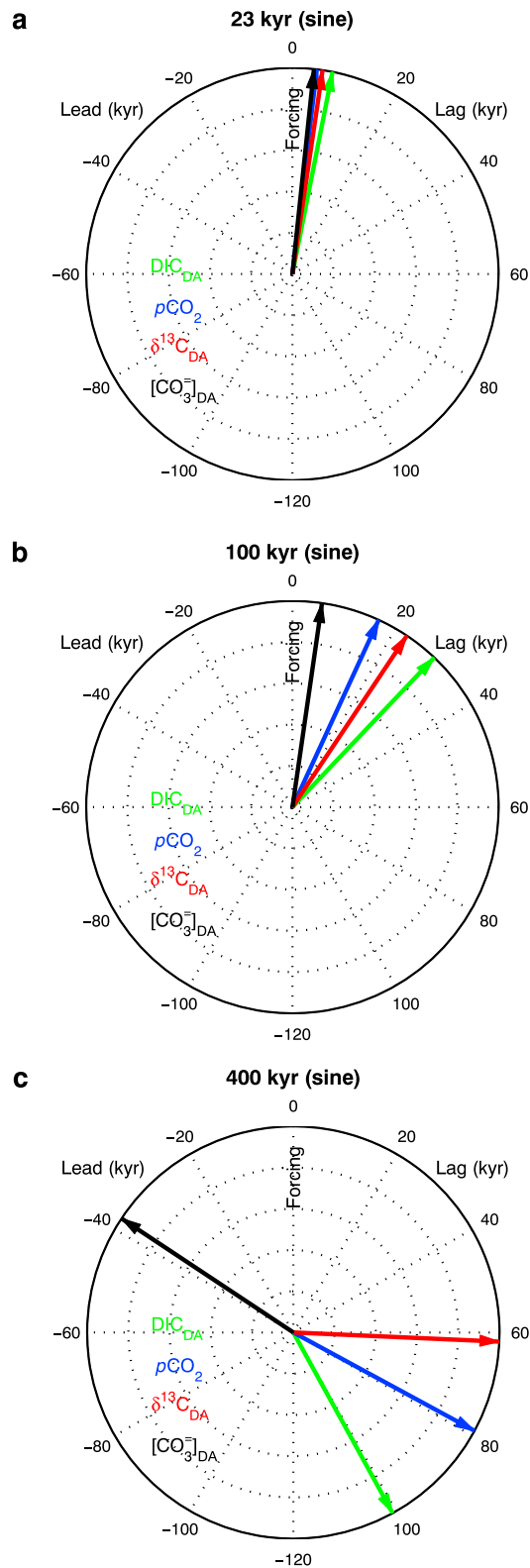
Figure 7. Polar plots (phase wheel) to illustrate phase relationships between C cycle variables from LOSCAR runs with sinusoidal forcing. Phase angles are expressed in terms of leads and lags (kyr), all relative to the forcing (phase angle = 0). (a) 23 kyr, (b) 100 kyr, and (c) 400 kyr forcing. For example, at 400 kyr, δ^{13}C in the deep Atlantic (DA) lags the forcing by ~60 kyr. Note that the model-computed phase relationships depend strongly on model setup and parameters; they can also be changed by applying additional forcing (section 5.3.1).

observation that sediment dissolution appears to lead the carbon input at Site 1262 on 400 kyr time scale (section 6.1). For the model-data comparison, however, we will mostly focus on the phasing between δ^{13}C and pCO$_2$ (i.e., T/δ^{18}O, section 5.2).

5.1.1. δ^{13}C-Eccentricity Lag

Combining the model results presented in section 5.1 and Appendix B shows that the δ^{13}C-forcing lag is a simple accumulation effect plus different total C and ^{13}C response times. As a corollary, the lag increases with the forcing period and approaches ~60 kyr at $\mathcal{T} = 400$ kyr (Figure 7). Considering the δ^{13}C-forcing lag only and equating our 400 kyr forcing function to eccentricity, our mechanism hence provides an explanation for the observed δ^{13}C-eccentricity lag of ~30–60 kyr at the 400 kyr period in Paleocene, Oligocene, and Miocene sections [*Zachos et al.*, 2001b; *Holbourn et al.*, 2007; *Pälike et al.*, 2006b; *Westerhold et al.*, 2011]. Note that due to major differences in boundary conditions, we restrict the discussion of other epochs here to the δ^{13}C-forcing lag only. At the 100 kyr period, the model lag (~20 kyr) coincides with the upper end of observations (0–20 kyr).

5.2. LOSCAR's Response to Insolation Forcing: Carbon Burial Only

In the following, we apply the same insolation forcing to LOSCAR that was used to drive the simple model (flavor $\boldsymbol{w}_d = [1\ 0.5\ 0.5\ 0.5]$, Figure 4). It suffices to run the model over 5 Myr because results and spectra are very similar over 5 or, e.g., 10 Myr (although 5 Myr improves intelligibility of figures). It is also immaterial whether insolation forcing is used for $t = [-60, -55]$, $[-55, -50]$, or $[-5, 0]$ Ma (section 4). The modeling goal here is to match the general variability amplitude, noise level, and spectrum of the benthic isotope records, not to replicate specific chronological features. Hence, the time interval of, for instance, the model-data-δ^{13}C comparison below is arbitrary. The forcing amplitude has little effect on the shape of the spectrum and, for the simple model, only needs to be adjusted relative to the noise level. However, for LOSCAR the forcing amplitude largely determines the magnitude of the δ^{13}C cycles. Hence, we adjust the forcing amplitude in LOSCAR such that the model's δ^{13}C of deep Atlantic DIC is compatible with the benthic δ^{13}C record at Site 1262. As above, we force the carbon flux due to organic carbon burial:

$$F_{gb} = F_{gb}^0 \left[1 - \gamma \mathcal{I}_0 \right], \tag{7}$$

where γ is the forcing amplitude and $\mathcal{I}_0$ is the normalized insolation forcing. Again, the negative sign produces δ^{13}C minima in the exogenic reservoir at eccentricity/insolation maxima, consistent with the data records.

When using the model-data comparison to adjust the forcing, it is important that in the current approach, the model was not set up to simulate, for instance, the hyperthermals and smaller events associated with negative carbon isotope excursions (CIEs). The large observed CIEs during hyperthermal events such as the PETM and ELMO indicate massive, additional carbon release (note though that these events were removed from the data time series for spectral analysis; for further information, see Figure S6). We take this observation as evidence for episodic, additional release of isotopically light carbon (including H1 and I1 not simulated by the model) that is distinct from the proposed quasiperiodic carbon release and removal in response to long-term orbital forcing. As a result, the distribution of observed, detrended δ^{13}C values should be skewed toward negative values relative to the background cycle and hence relative to the model's δ^{13}C distribution, which is indeed the case (Figure 8, both adjusted to mean zero). For a proper model-data comparison we therefore ignore the tail on the negative side of the observed distribution and assume that orbital forcing alone would produce a roughly symmetric δ^{13}C distribution around the data mean (similar to the model). The target range of δ^{13}C values (or width of distribution) based on the observed, detrended benthic record at Site 1262 is then given by twice its positive range, i.e., about ±0.4‰ (Figure 8). To roughly match this distribution width in LOSCAR, the forcing amplitude was set to $\gamma = 0.29$ (Figure 8). This means the absolute minimum C_{org} burial over 5 Myr, for example, is ~30% lower than its initial value (no noise, equations (2) and (7)). However, typical changes over the larger half-precession cycles are only ~10–20%.

Forced with this insolation-driven C_{org} burial plus noise (see below), we calculated various carbon cycle parameters with LOSCAR over 5 Myr, including atmospheric CO$_2$ (Figure 9). Starting at an initial steady state value of 1000 ppmv, the model predicts maximum CO$_2$ variations of about ±100 ppmv due to orbital forcing of C_{org} burial at a dominant period of ~405 kyr. From the model output, we also calculate a "pseudo"-$\Delta\delta^{18}$O:

$$\Delta\delta^{18}\text{O} = -4.80^{-1} \times (T - T_0), \tag{8}$$
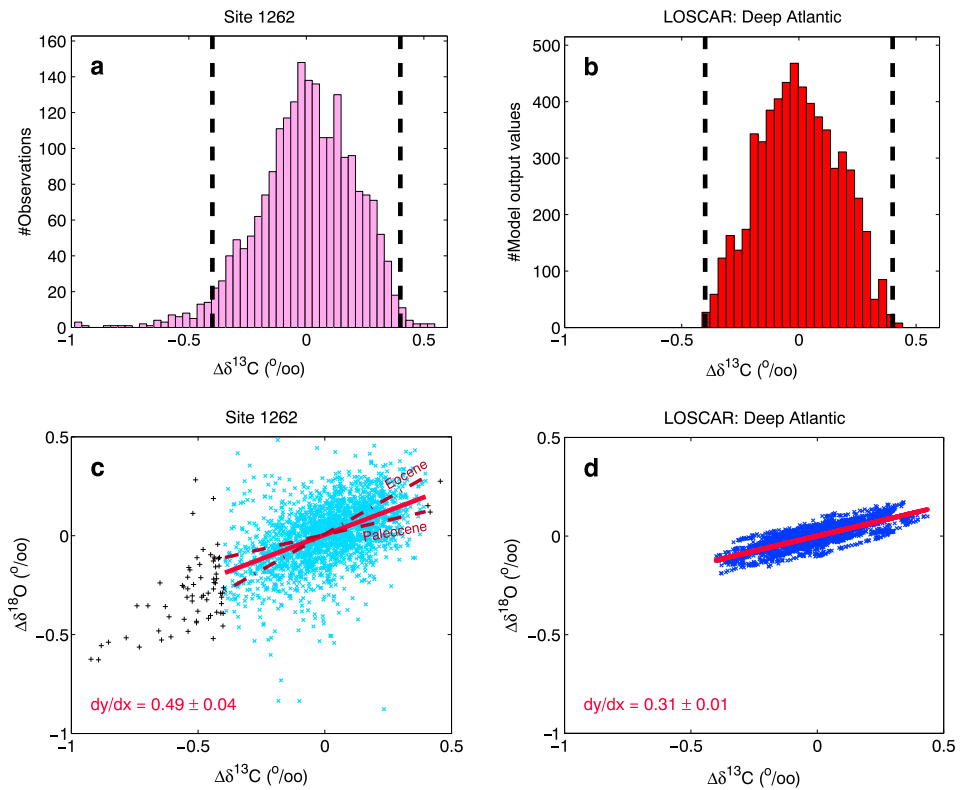
Figure 8. Data-model comparison between benthic isotope records at Site 1262 and insolation + noise-forced LOSCAR output (C_{org} burial only). (a) Histogram of observed $\delta^{13}C$ values relative to the mean ($\Delta\delta^{13}C$). (b) Same for LOSCAR output from 5 Myr runs (Figure 9, Deep Atlantic). Note that #(model output values) $\ll$ #(time steps) and that LOSCAR uses adaptive time step control. (c) Observed $\Delta\delta^{18}O$ versus $\Delta\delta^{13}C$ and slope. Solid red line: all data for $\delta^{13}C = [-0.4\ 0.4]$‰; dashed/dot-dashed red line: Paleocene/Eocene data only (see section 6.2 and Figure 12). (d) Same for LOSCAR output. Slope in Figure 8c is similar whether black crosses are included or excluded (see text).

where the factor -4.80 K/‰ converts between temperature change and foraminiferal $\Delta\delta^{18}O$ [*Bemis et al.*, 1998]. T and T_0 is Earth's surface temperature at time t and t_0, in LOSCAR estimated as

$$(T - T_0) = S_{2x} \times \ln\left(pCO_2/pCO_2^0\right) / \ln(2) \qquad (9)$$

and including a time delay for different ocean depth levels [*Zeebe*, 2012]. S_{2x} is the global surface temperature change per CO_2 doubling—on orbital time scales assumed to reflect Earth System Sensitivity (ESS)—and taken here as $S_{2x} = 5$ K.

Comparison of the computed pseudo-$\Delta\delta^{18}O$ and $\Delta\delta^{13}C$ in the model's deep Atlantic box versus observed benthic isotope ratios at Site 1262 indicates two important differences (Figure 8). First, the scatter in the data (particular $\delta^{18}O$) is much larger than in the model. This is expected because in the model, we only imposed noise on the carbon burial ($\delta^{13}C$), not on T ($\delta^{18}O$) independently. Also, the data are affected by suborbital temperature fluctuations, proxy noise, analytical errors, etc., not included in the model. Second, the observed slope of $\Delta\delta^{18}O$ versus $\Delta\delta^{13}C$ ($\sim$0.5) is significantly larger than in the model ($\sim$0.3), when forced by C_{org} burial only (Figure 8). Note that the observed slope of $\sim$0.5 is largely independent of whether the $\Delta\delta^{13}C$ values < -0.4‰ and > 0.4‰ that were removed for the $\Delta\delta^{13}C$ target range are included or excluded (slope = 0.52 versus 0.49).

Thus, while our simulations forced only by C_{org} burial mostly capture the observed amplitude of benthic $\delta^{13}C$ variations and the features of the $\delta^{13}C$ spectrum (Figure 9), the model results for $\Delta\delta^{18}O$ suggest that something is missing. The modeled temperature response and its noise amplitude appear too small. Also, the simple 400 kyr burial-only forcing (Figure 7) produces a $\delta^{13}C$ lead over pCO_2, i.e., over $T/\delta^{18}O$. (Cross-spectral analysis of the insolation-forced LOSCAR results indicates a similar phasing at 405 kyr.) However, the data suggest the reverse, a $\delta^{18}O$ lead over $\delta^{13}C$ [*Littler et al.*, 2014]. Hence, it appears that additional forcings and/or
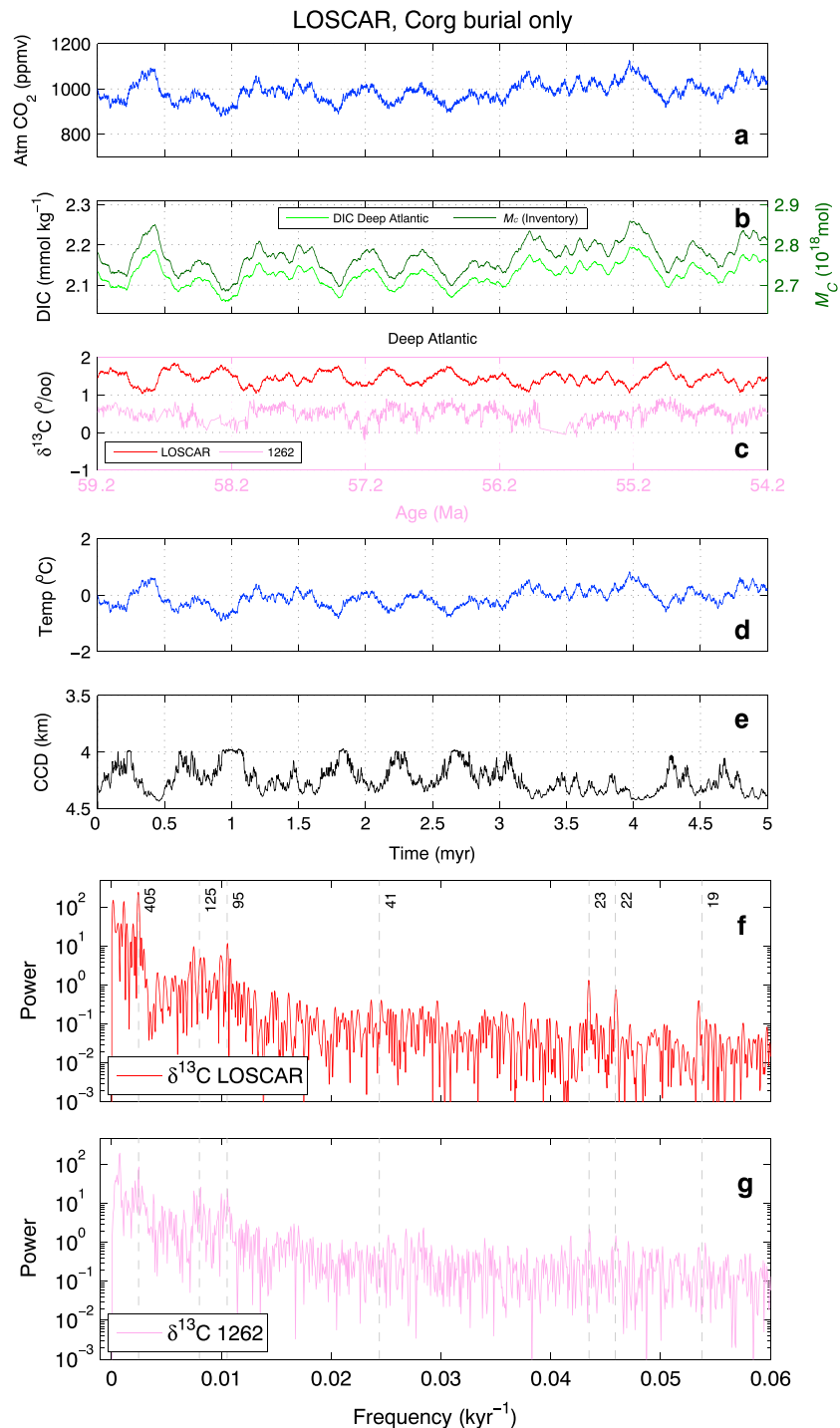
Figure 9. LOSCAR's atmospheric and deep Atlantic response to insolation + noise forcing (Figures 4a and 4b) for C_{org} burial only. (a) Atmospheric CO_2. (b) Dissolved inorganic carbon and ocean DIC inventory (M_C). (c) $\delta^{13}C$, deep Atlantic box and at Site 1262 (detrended, arbitrary xy offset). The time interval of model-data comparison is arbitrary due to uncertain orbital solution (section 4). (d) Temperature (equation (9)). (e) CCD. Figures 9c–9e show output for LOSCAR's deep Atlantic box. (f) FFT power spectrum of model $\delta^{13}C$ shown in Figure 9c. Vertical dashed lines indicate periods (kyr). (g) FFT power spectrum of benthic $\delta^{13}C$ record at Site 1262.

feedbacks need to be included in the model simulations to make better sense of the data. This is not surprising because the burial-only scenario is based on various simplifying assumptions (listed in section 6).

5.3. Additional Forcings/Feedbacks
5.3.1. Eccentricity and Global Insolation

One direct climate forcing affecting the total incoming radiation on Earth on 100 kyr time scale is variations in Earth's orbital eccentricity (e):

$$S_0 = \frac{S_a}{\sqrt{1 - e^2}} , \qquad (10)$$

where S_0 and S_a are the energy per unit area and time received at mean radius of Earth's actual orbit and at constant radius a (Earth's semimajor axis), respectively [*Berger and Loutre*, 1994]. S_0 is often called the solar constant, for the present set here to 1368 W m^{-2}. Variations in S_0 due eccentricity (ΔS_0) are relatively small ($\lesssim 3$ W m^{-2}) because e only varies, for instance, between ~ 0 and ~ 0.07 over the past 60 Ma. However, these changes are not unimportant because among the three orbital parameters, only eccentricity alters the annual mean global insolation. Note that while eccentricity changes are also underlying the insolation forcing applied to C_{org} burial (section 5.2), the forcing is based on insolation at distinct latitudes (not global) and was not applied to temperature.

The climatically relevant forcing is actually $\Delta S_0 (1 - 0.3)/4$, which takes into account Earth's albedo and the fact that the absorbed energy on a circle (area πR^2) is distributed over the surface of a sphere ($4\pi R^2$). Hence, we take as the radiative forcing ΔF_S:

$$\Delta F_S = [S_0(t) - S_0(t_0)] \times (1 - 0.3)/4 , \qquad (11)$$

which varies at maximum by $\sim 3 \times (1 - 0.3)/4 = 0.5$ W m^{-2}. To estimate the global surface temperature change associated with ΔF_S,

$$\Delta T = \lambda_S \, \Delta F_S , \qquad (12)$$

the sensitivity parameter λ_S needs to be evaluated. Studies based on observations of the 11 year solar cycle, energy balance models, and general circulation models (GCMs) suggest that $\lambda_S \simeq 0.5 - 1.0$ K (W m^{-2})$^{-1}$ [*Graves et al.*, 1993; *Hansen et al.*, 1997; *Lean and Rind*, 2001; *Tung et al.*, 2008]. However, these studies mostly consider short-term, transient changes (decades) rather than long-term equilibria (>10 kyr), and in case of GCMs only fast feedbacks. Over 100 kyr, additional feedbacks are likely active, which increase λ_S [e.g., *Zeebe*, 2013b] and we take λ_S as 1.4 K (W m^{-2})$^{-1}$, twice the value suggested by GCMs.

The additional, global solar forcing has two effects on our model results. First, it raises the maximum temperature amplitude by at most $\Delta T = \lambda_S \Delta F_S \simeq 1.4 \times 0.5 = 0.7$ K (if responses to forcings add linearly, no amplification). Second, it changes the phase relationship between $\delta^{18}O$ and $\delta^{13}C$ with a tendency toward $\delta^{18}O$-lead because temperature ($\delta^{18}O$) now responds directly to solar forcing. Indeed, LOSCAR runs with added global solar forcing displayed a $\delta^{18}O$-lead over $\delta^{13}C$ of several kiloyears at periods of 100 and 400 kyr (cross-spectral analysis, Figure S7). Also, the maximum temperature amplitude increased by ~ 1 K (amplified by T-solubility-CO_2 feedback). However, the modeled slope of $\Delta\delta^{18}O$ versus $\Delta\delta^{13}C$ (cf. Figure 8) only increased from 0.31 to 0.38, still short of the observed slope of ~ 0.5. Because the added global solar forcing sufficiently improves the model's $\delta^{18}O$-$\delta^{13}C$ phase relationship, we refrain from further increasing or including additional forcings. Instead, we add one more ingredient to the model simulations in form of a feedback to increase the modeled $\Delta\delta^{18}O$-$\Delta\delta^{13}C$ slope (section 5.3.2).

5.3.2. Temperature-Dependent Organic Matter Remineralization

As discussed in section 5.1, during CCD shoaling when $CaCO_3$ burial is reduced, weathering fluxes cause a rise in ocean alkalinity (TA), which speeds up the stabilization of the saturation state and causes a lead of pCO$_2$ over DIC. By the same mechanism, the alkalinity increase also reduces the magnitude of the pCO$_2$ rise. In other words, the amplitude of the pCO$_2$ cycle (and hence temperature) is damped by the TA/DIC response of the system. This negative feedback is most pronounced at the 400 kyr period, which provides enough time to significantly change ocean TA and DIC inventories. As a corollary, any positive feedback enhancing, say, an initial DIC rise and/or delaying the TA increase would amplify the pCO$_2$-temperature cycle. Several carbon cycle processes could provide such a positive feedback, for instance, changes in the production and export of C_{org} and/or $CaCO_3$ from the ocean's surface layer, changes in shelf- versus deep ocean $CaCO_3$ deposition, and more [e.g., *Ridgwell and Zeebe*, 2005]. Here we focus on the temperature-dependent remineralization of organic matter in the water column [e.g., *Matsumoto*, 2007; *Kwon et al.*, 2009; *Zeebe*, 2013a].
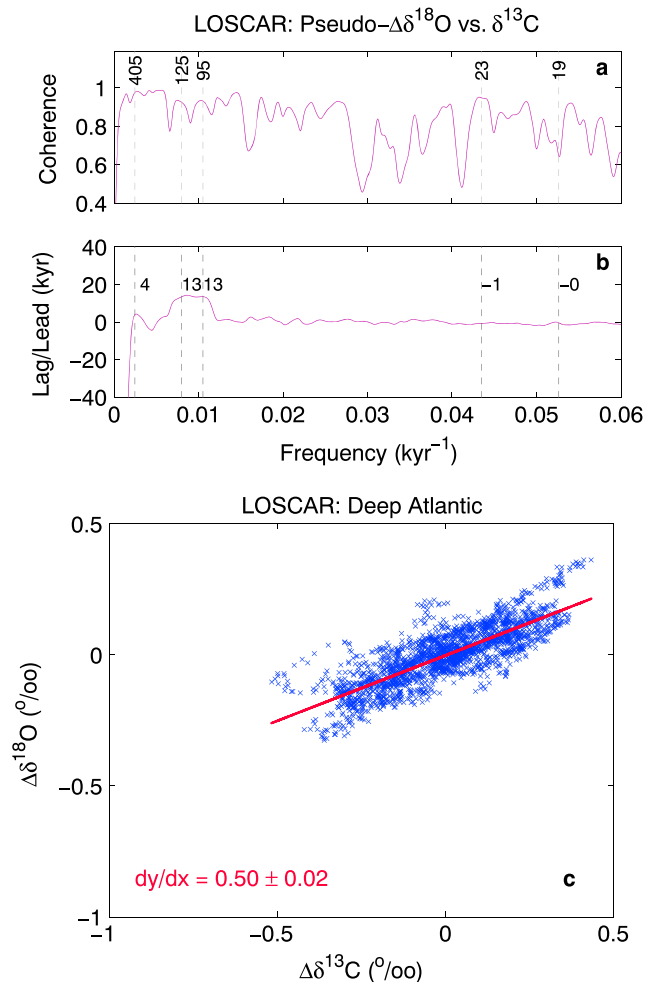
Figure 10. Coherence, phase lag, and slope of $\Delta\delta^{18}O$ versus $\Delta\delta^{13}C$ of insolation + noise-forced LOSCAR runs for C_{org} burial + global solar temperature + T-dependent remineralization ($Q10$ rule). Coherence and phase (leads/lags) were computed using MATLAB's cross power spectral density estimates based on Welch's method (pwelch.m, cpsd.m) with eight windows and 50% overlap. (a) Coherence. Vertical dashed lines indicate periods ($\mathcal{T}$, kyr). (b) Phase. Numbers (kyr) next to dashed lines indicate leads/lags at $\mathcal{T}$, positive for $\Delta\delta^{18}O$ lead. (c) Slope (see Figure 8).

It is well known that metabolic rates are sensitive to temperature. For example, the so-called $Q10$-rule states that metabolic rates (R) roughly double for every 10 K increase in temperature:

$$R = R_0\,Q10^{(T-T_0)/10} \tag{13}$$

where $R_0 = R(T_0)$ and $Q10 = 2$. Thus, for, e.g., a 1 K temperature increase during P/E orbital cycles, rates would have increased by $2^{1/10} \simeq 7\%$ (the relative change is T-independent, the absolute is not; see section 6.2). A rise in oceanic C_{org} remineralization would slightly shift the release of respired CO_2 upward in the water column, which tends to increase atmospheric CO_2 (positive feedback). This feedback predominantly increases the amplitude of the pCO_2, T, and hence $\delta^{18}O$ response, rather than of $\delta^{13}C$, if controlled by the amplitude of a cyclic carbon flux. Interestingly, as the orbital cycles discussed here are superimposed on a long-term warming trend (Figure 12), the $Q10$ effect and hence the $\delta^{18}O$-$\delta^{13}C$ relationship should change over time (for discussion, see section 6.2). Note that the $Q10$ rule also applies to other metabolic rates that may represent various positive and negative feedbacks. The assumption here is that the sum of the feedbacks, including water column remineralization, results in a small net positive feedback.

In the standard LOSCAR version, 78% of C_{org} exported from the ocean's surface layer is remineralized within the upper 1000 m (intermediate fraction, $f_m = 0.78$). We implemented a simple response to temperature such that f_m increases (drops) by 1.5% points for a 1 K rise (fall). This rather small positive feedback was sufficient to increase the modeled $\Delta\delta^{18}O$-$\Delta\delta^{13}C$ slope from 0.38 to 0.50 (Figure 10), in agreement with the benthic
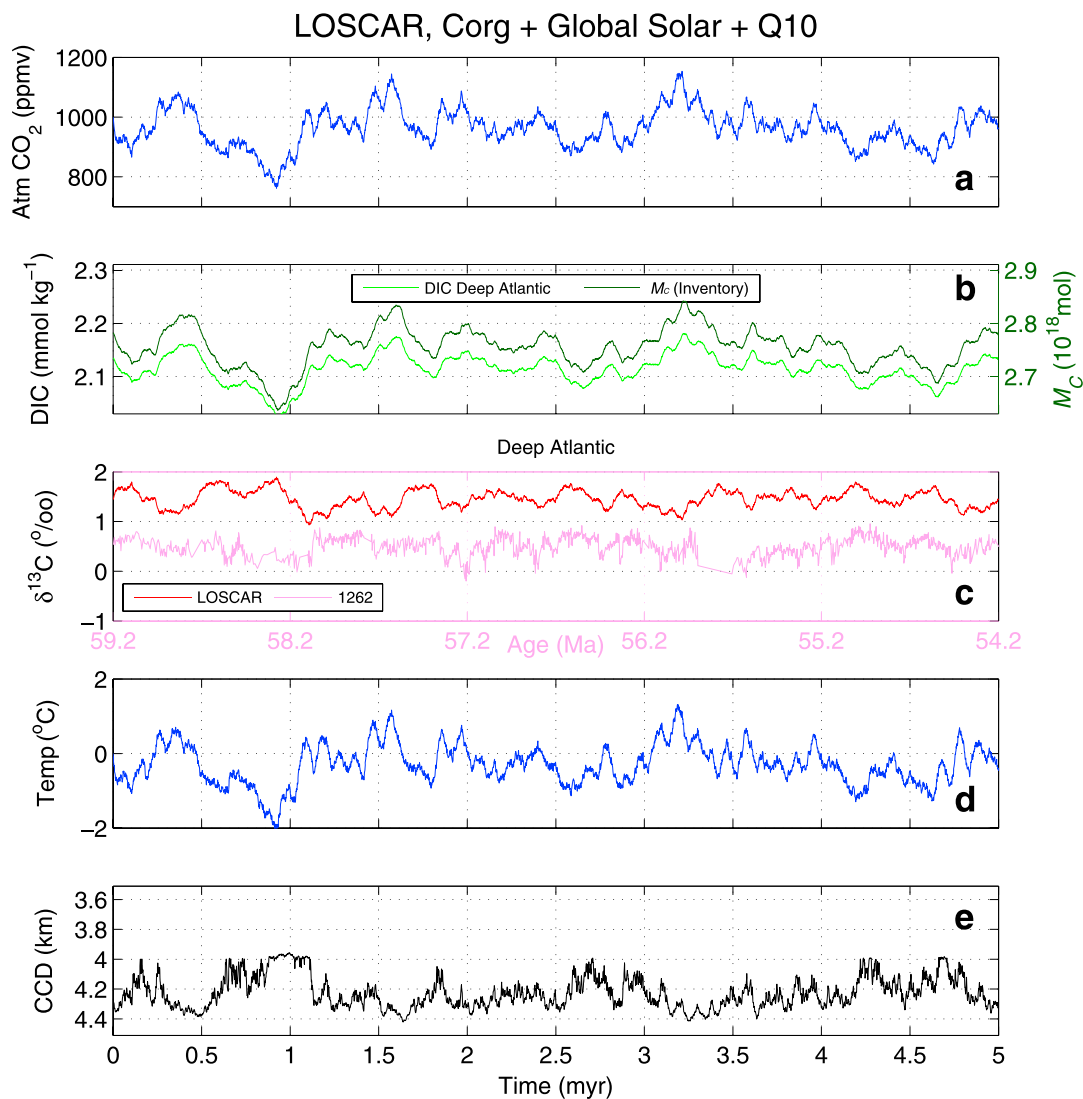
Figure 11. LOSCAR's response to insolation + noise forcing (Figures 4a and 4b) for C_{org} burial + global solar temperature + T-dependent remineralization (Q10 rule). Otherwise same as Figures 9a–9e. The time interval of model-data comparison in Figure 11c is arbitrary due to uncertain orbital solution (section 4).

isotope record's slope at Site 1262 (Figure 8). As a box model, LOSCAR is probably more sensitive to changes in remineralization depth than more complex models [cf. *Matsumoto*, 2007; *Kwon et al.*, 2009; *Zeebe*, 2013a]. However, the sensitivity is of secondary importance here because the results are tuned to observations (different model would require different f_m change).

In summary, adding global solar climate forcing and temperature-dependent remineralization to the basic C_{org}-burial forcing improves LOSCAR's $\Delta\delta^{18}O$-$\Delta\delta^{13}C$ phase and slope relative to the observed values of the benthic isotope records at Site 1262. The insolation-forced LOSCAR runs that include all three processes give maximum CO_2 cycles at 405 kyr of about ±200 ppmv (Figure 11). We offer the above mechanisms as possible solutions that are consistent with observations, including the time evolution of the $\Delta\delta^{18}O$-$\Delta\delta^{13}C$ slope (see section 6.2). However, we are fully aware that our solution is not unique and that other forcings and feedbacks are possible [e.g., *Pälike et al.*, 2006b; *Ma et al.*, 2011; *Russon et al.*, 2010; *Wang et al.*, 2014], particularly those directly responding to global temperature.

6. Discussion

Our modeling of the Paleocene-Eocene orbital cycles forced by C_{org} burial only (section 5.2) is based on several fundamental assumptions. These include the following: (1) insolation directly forces carbon cycling only;

pCO$_2$ and temperature variations are a response to that, i.e., no direct climate forcing through insolation (which we know is not the case). (2) No additional feedbacks are active, e.g., no long-term changes in ocean circulation, biological pumps, nutrient cycles such as P/O$_2$ burial/weathering, effects on rain ratio, and respiration. We also assumed that (3) the long-term carbon flux imbalance is caused by C_{org} burial with a distinct δ^{13}C signature (as opposed to other sources/sinks, including methane; see below) and (4) LOSCAR's entire deep Atlantic box properly represents conditions at Site 1262. To improve agreement with observations, we then relaxed assumptions (1) and (2) and included additional forcings and feedbacks but emphasize that these mechanisms do not necessarily represent a unique solution (section 5.3).

Our organic carbon burial scenario assumes a $\delta^{13}C_{org}$ value of -23‰. If a lighter carbon source (e.g., more methanogenic) was involved, then the carbon flux amplitude would be substantially reduced to produce the same exogenic δ^{13}C cycle. However, long-term rhythmic methane scenarios are problematic for several reasons, whether of oceanic or terrestrial origin [e.g., *Dickens*, 2003; *Konijnendijk et al.*, 2011]. First, a smaller carbon flux would produce an even smaller response in pCO$_2$, T, and hence δ^{18}O and dramatically increase the mismatch between the observed $\Delta\delta^{18}$O-$\Delta\delta^{13}$C slope and the model (section 5.2). Note that a large fraction of CH$_4$ would have had to be oxidized to CO$_2$ to produce the δ^{13}C cycles seen in the record. Importantly, regarding potential temperature variations driven by atmospheric CH$_4$, radiative forcing per CH$_4$ doubling (W m^{-2}) is only 1/8 to 1/6 that for CO$_2$ doubling for concentrations between 1000 and 4000 ppbv CH$_4$ [*Myhre et al.*, 1998]. Second, invoking periodic dissociation of oceanic methane hydrates, for instance, would require an initial deep water temperature rise, which is linked to high-latitude deep water formation. A direct trigger mechanism via high-latitude forcing, viz., obliquity, is then difficult to construct because a significant obliquity signal is absent from the records (section 6.3). Instead, one would have to rely on indirect trigger mechanisms such as orbitally forced changes in low-/middle-latitude temperature/salinity as a driver for long-term cycles in deep water formation and temperature. A feasible mechanism for a rhythmic source of volcanic carbon (isotopically heavier than C_{org}) driven by orbital changes is unknown at present.

Regarding potential carbon sources, we also point out a fundamental difference between a long-term carbon flux imbalance and a rapidly discharging reservoir, say a carbon capacitor (though not necessarily related to methane [*Dickens*, 2003; *Komar et al.*, 2013]). For example, in our insolation-forced C_{org} burial scenario (equivalent to a net long-term C_{org} oxidation and burial imbalance), LOSCAR requires a moderate change in the net flux of typically less than 10–20% over a half-precession cycle ($\sim$10 Pg C kyr^{-1}). This represents a tiny fraction of the total organic long-term reservoir ($\sim$10^7 Pg C). In contrast, a carbon capacitor usually provides several orders of magnitude less storage capacity and would require discharging and recharging on the same time scale. Thus, modeling an orbitally forced carbon cycle with a capacitor would require careful assessment of mass balances and recharge times—such as storing/releasing several thousand Pg C over a 400 kyr cycle (see Figure 6a).

6.1. Sediment Dissolution Leading the Carbon Input?
Littler et al. [2014] analyzed the phasing between wt % coarse fraction (%CF) and δ^{13}C at Site 1262 and suggested that that at 405 kyr "carbonate dissolution occurred prior to the release of the reduced carbon." The %CF data should be taken with caution because of potential postdepositional sediment burn down and the fact that the phasing is inconsistent across different parts of the record [*Littler et al.*, 2014, Figure S7]. Nevertheless, our simulations provide an explanation for the surprising %CF-δ^{13}C phasing at Site 1262 (see section 5.1). If confirmed, improved and extended sediment dissolution records might help to provide constraints on highly sought after weathering parameters.

6.2. Long-Term Trends and $\Delta\delta^{18}$O-$\Delta\delta^{13}$C Slope
The late Paleocene-early Eocene orbital cycles are superimposed on a multimillion year warming trend and a decline in mean-δ^{13}C (Figure 12) [e.g., *Zachos et al.*, 2001a; *Bijl et al.*, 2009; *Komar et al.*, 2013]. This warming trend has potential implications for climate-carbon cycle feedbacks, including T-dependent remineralization (section 5.3.2). According to the Q10 rule, metabolic rates roughly double for every 10 K increase in temperature. Importantly, the absolute change in the rate also doubles every 10 K, just as the rate itself ($dR/dT = R \cdot \ln(2)/10$). For example, if $R(10 \deg C) = 100$ units, then R increases by 7 units between 10 and 11°C but by 14 units between 20 and 21°C. Thus, for a given δ^{13}C (and initial T) amplitude one would expect the remineralization feedback to strengthen as global temperatures increase across the late Paleocene-early Eocene. In other words, the δ^{18}O response and hence the observed $\Delta\delta^{18}$O-$\Delta\delta^{13}$C slope (Figure 8c) should
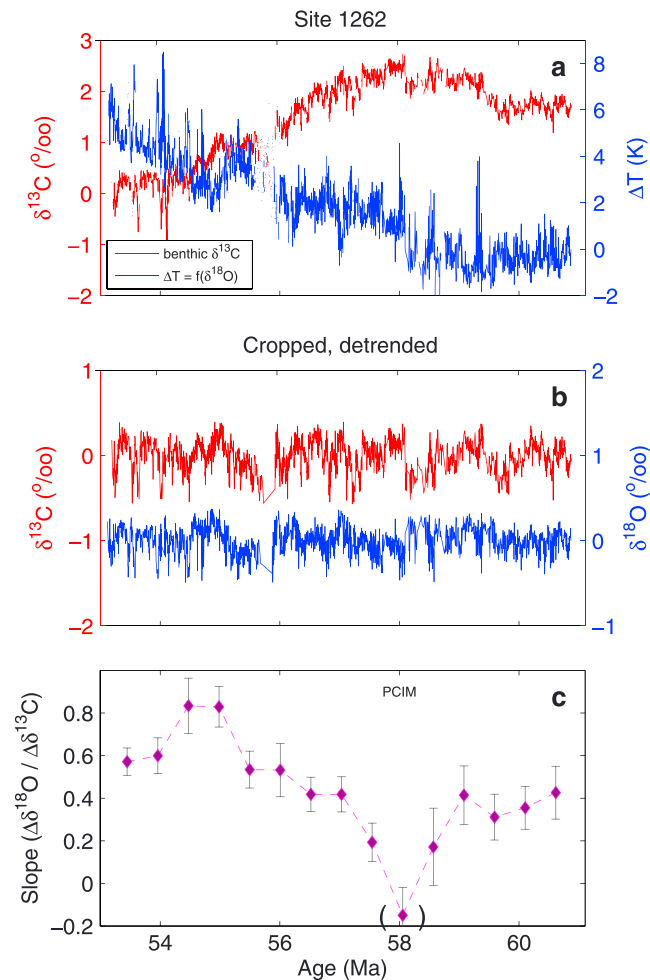
Figure 12. Long-term warming trend and $\Delta\delta^{18}$O-$\Delta\delta^{13}$C slope over time. (a) Benthic δ^{13}C and δ^{18}O from Site 1262 (δ^{18}O converted to ice-free temperature change using inverted equation (8) and $t_0 \simeq 61$ Ma). (b) Cropped and detrended time series. (c) Slopes for 15 bins of the data in Figure 12b, covering ~0.5 Myr each (20% overlap added for smoothing). Error bars are based on regression for each bin (see Figure 8). Note that the negative slope (in parentheses) prior/near the PCIM (Paleocene Carbon Isotope Maximum) is unlikely related to orbital variability.

increase over time (critical quantities for the slope here are Δ's based on detrended records, not long-term δ^{18}O-δ^{13}C; see supporting information).

To test this prediction, we binned the cropped and detrended benthic isotope data from Site 1262 into 15 sections (covering ~0.5 Myr each), added 20% overlap for smoothing, and calculated the slope for each bin (Figure 12c). Note that there could be a small effect of the long-term δ^{13}C decline on the $\Delta\delta^{13}$C amplitude (Figure 12a). All else being unchanged, the same carbon forcing amplitude would cause a slightly smaller $\Delta\delta^{13}$C at lower δ^{13}C$_{DIC}$. However, additional LOSCAR runs (not shown) predict this effect to reduce the slope by only ~0.05 for a 2.5‰ drop in δ^{13}C$_{DIC}$ (assuming constant ocean DIC inventory). The calculated temporal evolution of the $\Delta\delta^{18}$O-$\Delta\delta^{13}$C slope does not simply mirror the temperature trend (Figure 12c), yet most values during the warmer Eocene are significantly higher than at the beginning of the warming trend around 58 Ma. This observation is consistent with a stronger remineralization feedback at higher temperatures but does not rule out other scenarios.

The $\Delta\delta^{18}$O-$\Delta\delta^{13}$C relationship can be considered from two extreme perspectives. If, on the one hand, the cycles were mainly driven by a long-term carbon imbalance ($\Delta\delta^{13}$C), then the $\Delta\delta^{18}$O periodicity was a response whose magnitude would increase for any T-dependent feedback that behaves similar to remineralization. An alternative explanation is a shift toward heavier carbon isotope values of the carbon source going into the warmer Eocene (the same $\Delta\delta^{13}$C amplitude could be driven by more but "heavier" carbon, enhancing
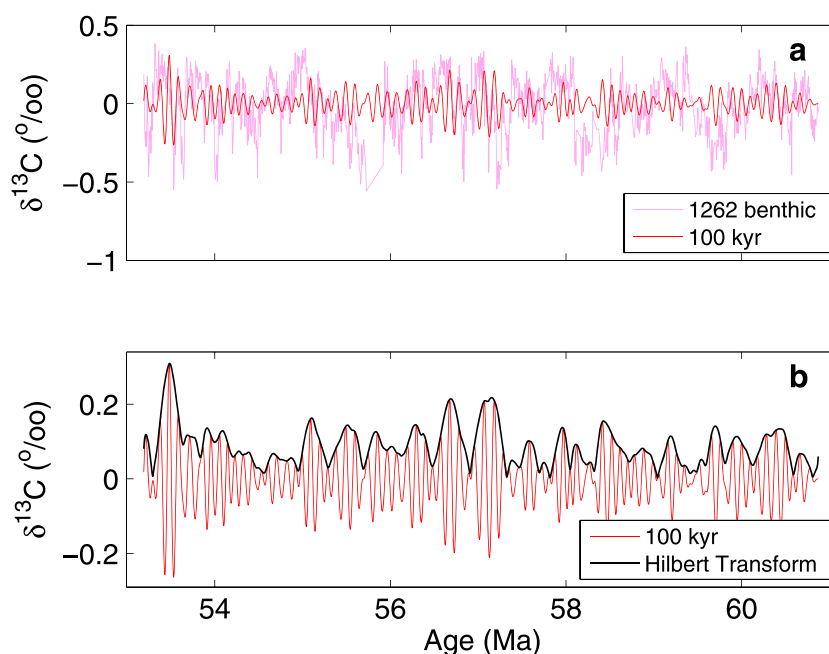
Figure 13. Example of low-frequency component analysis (slow-varying amplitude modulation) using the Hilbert transform. (a) Cropped and detrended benthic $\delta^{13}C$ from Site 1262 (light purple) and output from 100 kyr filter (red, $f = 0.01 \pm 0.003$ kyr, ±30%). (b) The 100 kyr filter and Hilbert transform (envelope).

the pCO$_2$ and $\Delta\delta^{18}$O response). Interestingly, if methane was involved, this would imply a less methanogenic source, for organic carbon, e.g., a shift toward marine versus terrestrial burial. If, on the other hand, the cycles were mainly driven by climate/temperature ($\Delta\delta^{18}$O), then the $\Delta\delta^{13}$C periodicity was a response, which was enhanced during the late Paleocene and diminished going into the early Eocene. The truth probably lies somewhere between these two extremes. Regardless of the driver, the consequence in terms of a changing carbon source/sink (if the cause) would be the same: a shift toward heavier values over time. Importantly, carbon source/sink here means a periodic process responding to orbital forcing, hence excluding a monotonic change in, e.g., volcanism, which does not affect the $\Delta\delta^{18}$O-$\Delta\delta^{13}$C slope. Currently, the available data do not allow us to distinguish between enhanced T-dependent feedbacks, shift in carbon source, and/or other causes. Theoretically, shifts in remineralization depth could be tested by reconstructing changes in vertical δ^{13}C$_{DIC}$ gradients [e.g., *John et al.*, 2013]. However, our model results suggest such changes to be subtle and possibly well within the error of the method.

6.3. High-/Low-Latitude Forcing, Obliquity, and Amplitude Modulation

As mentioned above, Paleocene-early Eocene (P/E) long-term records typically show very little or no power in the obliquity band around 41 kyr (cf., Figure 1), which is expected, given the absence of significant ice sheets [*Westerhold et al.*, 2007; *Zachos et al.*, 2010; *Westerhold and Röhl*, 2013; *Littler et al.*, 2014; *Meyers*, 2015]. Thus, it is also very unlikely that a tilt signal would be expressed at other, say, lower periods such as at 1.2 Myr due to amplitude modulation (AM) of obliquity as identified during the Oligocene-Miocene when substantial ice sheets were present [*Shackleton et al.*, 1999; *Pälike et al.*, 2006a]. Nevertheless, in this section we address two related questions: (1) Do long-term P/E carbon and oxygen isotope records display AM beats at the dominant obliquity variability periods of 1.2 Myr and ~170 kyr found in astronomical solutions? (2) What, if any, million-year beats can be found in these records? Addressing (1) is important for our proposed low-latitude forcing mechanism, which is based on the absence of obliquity signals in the P/E isotope records. Addressing (2) clarifies specifically whether the 2.4 Myr eccentricity beat [*Laskar et al.*, 2004; *van Dam et al.*, 2006] paced the P/E carbon cycle-climate system and, generally, how such million-year periodicity can be properly identified.

Cycles on million-year time scale are difficult to identify by direct spectral analysis of the data records. Detrending, intended to remove secular changes, interferes with long-term orbital trends and creates artificial peaks at the low-frequency end, depending on method and interval length [cf. also *Vaughan et al.*, 2014].
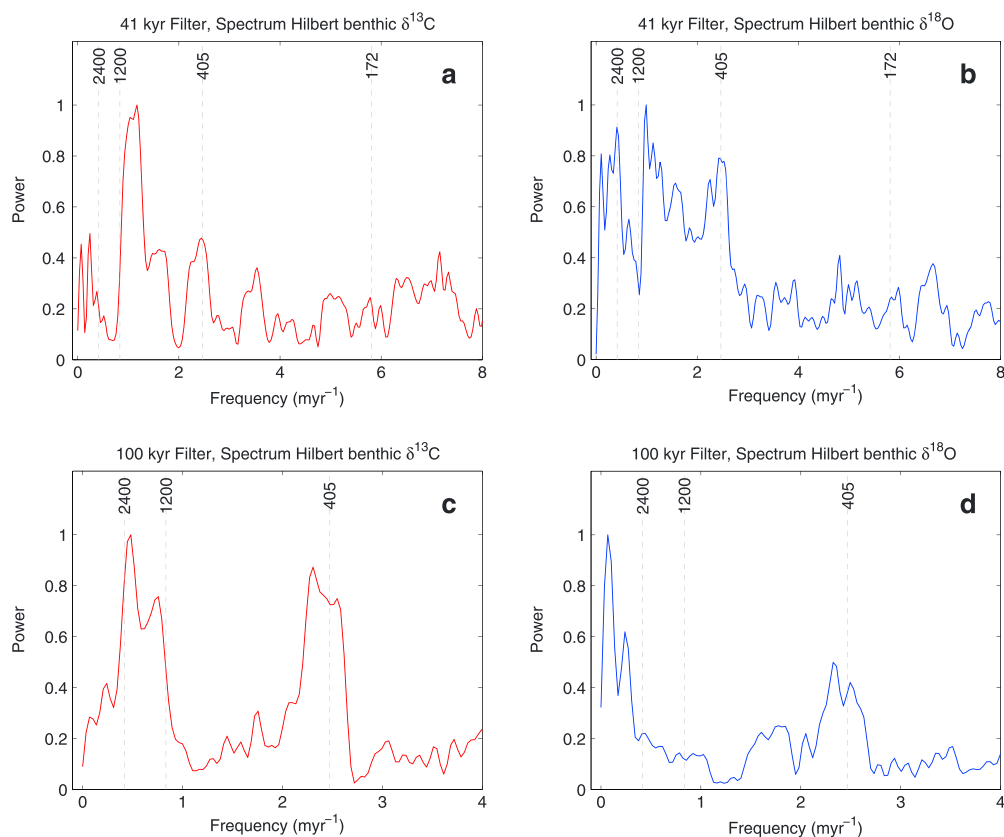
Figure 14. MTM spectra (time-bandwidth product = 2, tapers = 3) of Hilbert transforms of the filtered benthic δ^{13}C (red) and δ^{18}O (blue) records at Site 1262 (see Figure 13 for an example). (a and b) The 41 kyr filter (bandwidth ±30%). (c and d) The 100 kyr filter (±45%). Vertical dashed lines indicate periods (kyr). Note the different frequency (*x* axes) limits.

One solution to the AM problem is "complex demodulation" [*Bloomfield*, 2000; *Shackleton et al.*, 1999; *Pälike et al.*, 2006a], another by means of the Hilbert transform, used here (Figure 13) [*Hinnov*, 2000; *Boulila et al.*, 2012; *Meyers*, 2015; *Zeeden et al.*, 2015]. Note that we will not test the astronomical origin of potential AM cycles at, e.g., 170, 1,200, and 2,400 kyr using *Zeeden et al.*'s [2015] approach because our results below do not indicate such cycles in the records. We first detrend the 1262 benthic δ^{13}C record and then apply a 100 kyr band-pass filter ($f = 0.01 \pm 0.003$ kyr, ±30%, Figure 13a). Next, we apply a Hilbert transform to the filter output, which essentially extracts the envelope (slow-varying AM) of the 100 kyr component (Figure 13b).

The 405 kyr cycle is easily visible just from the graph of the Hilbert transform, as confirmed by the MTM spectrum (Figure 14c). There also appears a peak around 2.2 Myr — however, a Blackman-Tukey and periodogram analysis (not shown) puts this peak closer to 1.6–1.9 Myr. Moreover, the peak is not present in the corresponding δ^{18}O transform spectrum (Figure 14d) and is therefore unlikely an expression of the 2.4 Myr eccentricity beat. The Hilbert transform spectra of the 41 kyr filter output for δ^{13}C and δ^{18}O do not show prominent peaks at 1.2 Myr and ~170 kyr (Figures 14a and 14b). Note that these results are largely independent of the detrending and the filter applied (rectangular, Butterworth order 4–10). Indeed, varying the interval length for linear detrending between 5% and 50% of the record makes very little difference. We conclude that the 1262 P/E benthic isotope records show (1) no obliquity signal at ~41, ~170, and ~1200 kyr and (2) no conclusive eccentricity signal at ~2.4 Myr.

7. Summary

Detailed characterization of low- and high-frequency cyclic climate and carbon cycle variability in Paleogene deep-sea sequences has provided a unique opportunity to evaluate the sensitivity of the carbon cycle-climate system to orbital forcing over long time scales. Here we have used simple and complex carbon cycle models to examine the basic effect of different orbital forcing schemes and noise on the P/E carbon cycle. The system's

tendency to transfer spectral power from high to low frequencies can be explained by insolation transformations analogous to electronic AC-DC conversion (DC'ing). We propose that tropical insolation forcing and a long-term carbon imbalance in terrestrial organic burial/oxidation represent a viable link between astronomical forcing and the carbon cycle-climate system. However, our solution is unlikely to be unique and additional forcings/feedbacks are necessary to fully make sense of the P/E benthic isotope records at ODP Site 1262.

Our analysis shows that high-latitude mechanisms are unlikely drivers of orbitally paced changes in the late Paleocene-early Eocene Earth system. Furthermore, our simple 400 kyr sinusoidal forcing reveals a mechanism for the observed δ^{13}C-eccentricity lag of ~30–60 kyr at the 400 kyr period in Paleocene, Oligocene, and Miocene sections (section 5.1.1). We have also provided constraints on the origin and isotopic composition of a possible cyclic P/E carbon imbalance/source responding to astronomical forcing. Finally, we have presented the first estimates of orbital-scale variations in atmospheric CO_2 during the late Paleocene and early Eocene. Assuming a baseline CO_2 of 1000 ppmv, our estimated maximum CO_2 variations associated with the 405 kyr cycle are of order ±200 ppmv.

Appendix A: Minimum Frequency Error

The MTM spectrum of, e.g., the benthic δ^{13}C record at Site 1262 shows significant peaks at distinct frequencies (Figure 1c). Given that the age model/tuning is based on astronomical eccentricity cycles [*Westerhold et al.*, 2008], it would be circular to infer the 405, 125, and 95 kyr periods and their uncertainties from the spectrum. However, other peaks of interest (if present) and their periods may be determined from the spectrum such as circa 2.4 and 1.2 Myr and 170, 41, and 23 kyr. Importantly, even if the age model was free of errors, frequency estimation by spectral analysis itself has uncertainties, particularly given the large background noise in the current data set. Sometimes the Rayleigh resolution $f_R = 1/(N\Delta t)$ is used as an upper error bound but often greatly overestimates the error [*Montgomery and O'Donoghue*, 1999; *Kallinger et al.*, 2008].

Here we estimate a minimum uncertainty in a given frequency (f) due to a single forcing line at which a peak occurs in the spectrum (Figure 1) using Monte Carlo simulations [e.g., *Muller and MacDonald*, 2002]. Using the actual data resolution and noise level, we performed $M = 10,000$ simulations with a sinusoid (f_0) and red noise, generated by an AR(1) process plus white noise (different for each run) and a lag-one autocorrelation coefficient of ~0.7 as obtained from the fit to the observed spectrum (Figure 1c). The sine and noise amplitude were adjusted to replicate the observed signal-to-noise ratio of ~6 in the power amplitude at 405 kyr and ~100 kyr relative to the noise background in that frequency range. From the distribution of the obtained frequencies f_i ($i = 1, \ldots, M$) at the local MTM maximum around f_0, we calculate the standard deviation σ_f and take $\pm 2\sigma_f$ as the estimated minimum error. We found that independent of f_0, $\sigma_f \simeq 15\%$ of the Rayleigh frequency (f_R), which yields for the periods [2400 1200 170 41 23] kyr minimum errors $\Delta\mathcal{T} = |d\mathcal{T}/df|\Delta f = \Delta f/f^2 = \pm[225\ 56\ 1.1\ 0.07\ 0.02]$ kyr. Note that these are *minimum* errors, assuming that the forcing corresponding to each f_0 is represented by a single line. Resolving two forcing lines around f_0 is limited by the MTM bandwidth, $p \cdot f_R$ ($p = 2$ here), which gives $\Delta\mathcal{T} = \pm[1500\ 375\ 7.5\ 0.44\ 0.14]$ kyr for the above periods. For the short eccentricity cycles and precession periods, for instance, we would have 125 ± 4, 95 ± 2, 23 ± 0.14, and 19 ± 0.1 kyr. These uncertainties suggest that single forcing lines can be accurately determined and two lines be separated at high frequencies (say periods $\mathcal{T} \lesssim 10^5$ yr), but not at low frequencies ($\mathcal{T} \gtrsim 10^6$ yr).

Appendix B: Large δ^{13}C Lead Over DIC

For the sinusoidal forcing (section 5.1), LOSCAR's carbon isotope ratio of DIC (δ^{13}C) consistently leads DIC — by up to ~40 kyr at the 400 kyr forcing. Cross-spectral analysis (not shown) of the insolation-forced LOSCAR results (C_{org} burial only) indicates a similar phasing at 405 kyr. While some leads/lags are to be expected between DIC and DI^{13}C, a DIC-δ^{13}C lag of ~40 kyr appears surprisingly large. First, it is important to recall that δ^{13}C reflects the *ratio* of DI^{13}C/DIC (=: C'/C). It can be shown that even small leads/lags between two sinusoidal C', C can produce large leads/lags in the ratio C'/C relative to C' and C. Thus, we will focus here on identifying leads/lags between C' and C (those are substantially magnified in δ^{13}C). Note also that a proper mass balance approach (as in LOSCAR) integrates C and C' as tracers, not δ^{13}C.

It is known that total C and ^{13}C have different characteristic time scales, for instance, during air-sea gas exchange [*Broecker and Peng*, 1974; *Jones et al.*, 2014; *Galbraith et al.*, 2015]. However, the C'-C and C-δ delays (x-y delay means x lags y) are typically about a decade and a few centuries for gas exchange, respectively,
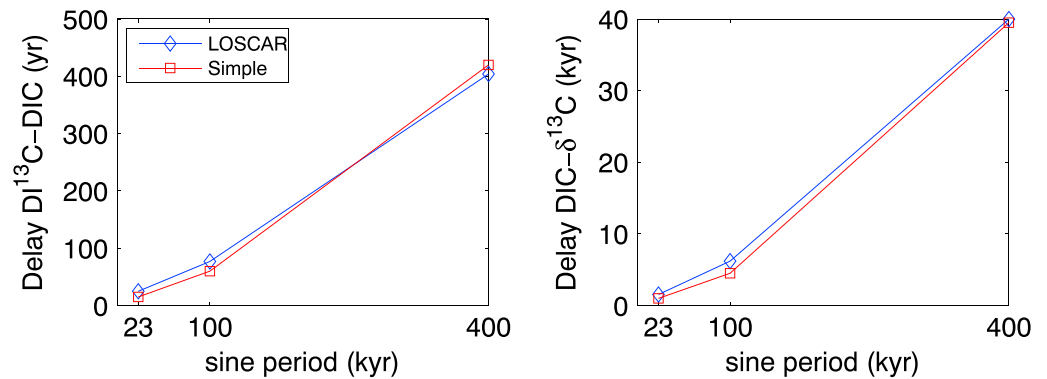
Figure B1. Leads/lags in model C and ^{13}C response to 23, 100, and 400 kyr sinusoidal forcing in LOSCAR (blue) and the simple 1-box ocean-sediment model (red). Note the different y scales (yr versus kyr). Lines are drawn just to aid the eye (relationship is nonlinear).

not millennia (tested in LOSCAR). It turns out that the large C-δ delays for sinusoidal forcing are caused by different long-term dynamics for C and C' during sediment burial and ocean inventory adjustment. Consider the following simplified 1-box ocean-sediment system, initially without forcing (equations for ocean tracers only):

$$V\frac{dC}{dt} = F - r + D \tag{B1a}$$

$$V\frac{dC'}{dt} = F' - r' + D' \tag{B1b}$$

$$V\frac{dTA}{dt} = (F - r + D) \times 2 \tag{B1c}$$

where V is volume, F is the riverine flux, r is the CaCO$_3$ (calcite) rain, D is sediment dissolution (burial = rain − dissolution), TA is alkalinity, and primes denote ^{13}C quantities.

For total C (as in LOSCAR), dissolution $D = k(c_s - c)^n$ where c_s and c is the carbonate ion concentration at calcite saturation and in the bottom water, respectively ($D = 0$ for $c > c_s$; k and n are dissolution parameters [*Zeebe*, 2012]). However, for C' the dissolution flux is simply the sediment ^{13}C/C ratio (R_{sd}) times the total dissolution, $D' = R_{sd}D$. In other words, total C controls the chemistry and hence the total mass of calcite dissolved, while all ^{13}C contained in that mass is simply returned to the bottom water. Another important difference is that the rain for ^{13}C (say constant for C) depends on the actual C'/C ratio in the ocean: $r' \simeq (C'/C)r$ (ignoring fractionation and surface-deep gradients). Using $F' = FR_{std}$, we have

$$V\frac{dC}{dt} = F - r + D \tag{B2a}$$

$$V\frac{dC'}{dt} = R_{std}F - (r/C)\,C' + R_{sd}D\,, \tag{B2b}$$

which shows that C and C' have very different dynamics (time constants). The response time for C is controlled by dissolution via the dependency of [CO$_3^{2-}$] on DIC and TA, i.e., the calcite compensation time scale (τ) of a few millennia applies (assuming F and r constant). In contrast, the long-term response for C' (once C and dissolution is constant) is proportional to C' itself with decay constant $\lambda' = r/(CV)$, which derives from $dC'/dt \simeq -r/(CV) \cdot C'$. This gives a time constant $\tau' = CV/r \simeq CV/F \simeq 200$ kyr. Thus, while C' also responds during calcite compensation, the long-term ^{13}C steady state is only established when the ocean's carbon isotope ratio has adjusted so that the burial ^{13}C/C ratio again equals that of the input. Briefly, in this simple view, ocean chemistry controls the total C response, while the residence time controls the ^{13}C response.

The fact that C and C' have different time constants also means different responses to forcing. For example, C' responds slightly more slowly to the sinusoidal forcing than C (section 5.1) because of the additional long-term adjustment discussed above. As a result, the C' response is delayed relative to C; e.g., the C' maximum occurs up to a few centuries after the C maximum (Figure B1). In turn, the centurial C'-C delay leads to a large C-δ delay (not δ-C delay!) of up to 40 kyr at the 400 kyr forcing. Again, the magnitude and direction of the δ-lead/lag (reflecting the C'/C ratio) may appear counterintuitive but can easily be understood by plotting the ratio of

two sinusoids such as $[C_0' + a' \sin(\omega t')] \, / \, [C_0 + a \sin(\omega t)]$ (not shown), where a, a' are constants, $t' = t - t_0$, and t_0 is a small time offset. The results of the simple model presented here are consistent with those of LOSCAR (Figure B1).

References

Abels, H. A., V. Lauretano, A. E. van Yperen, T. Hopman, J. C. Zachos, L. J. Lourens, P. D. Gingerich, and G. J. Bowen (2016), Environmental impact and magnitude of paleosol carbonate carbon isotope excursions marking five early Eocene hyperthermals in the Bighorn Basin, Wyoming, *Clim. Past*, *12*, 1151–1163, doi:10.5194/cp-12-1151-2016.

Ashkenazy, Y., and H. Gildor (2008), Timing and significance of maximum and minimum equatorial insolation, *Paleoceanography*, *23*, PA1206, doi:10.1029/2007PA001436.

Bemis, B. E., H. J. Spero, J. Bijma, and D. W. Lea (1998), Reevaluation of the oxygen isotopic composition of planktonic foraminifera: Experimental results and revised paleotemperature equations, *Paleoceanography*, *13*, 150–160.

Berger, A., and M. F. Loutre (1994), Precession, eccentricity, obliquity, insolation and paleoclimates, in *Long-term Climatic Variations*, edited by J.-C. Duplessy and M.-T. Spyridakis, pp. 107–151, Springer, Berlin, doi:10.1007/978-3-642-79066-9_5.

Berger, A., M. F. Loutre, and J. L. Mélice (2006), Equatorial insolation: From precession harmonics to eccentricity frequencies, *Clim. Past*, *2*, 131–136.

Bijl, P., S. Schouten, H. Brinkhuis, A. Sluijs, G.-J. Reichart, and J. C. Zachos (2009), Palaeogene temperature evolution of the Southwest Pacific Ocean, *Nature*, *461*, 776–779, doi:10.1038/nature08399.

Bloomfield, P. (2000), *Fourier Analysis of Time Series: An Introduction*, 2nd ed., 261 pp., John Wiley, New York.

Bosmans, J. H. C., S. S. Drijfhout, E. Tuenter, F. J. Hilgen, and L. J. Lourens (2014), Response of the North African summer monsoon to precession and obliquity forcings in the EC-Earth GCM, *Clim. Dyn.*, *44*, 279–297, doi:10.1007/s00382-014-2260-z.

Bosmans, J. H. C., F. J. Hilgen, E. Tuenter, and L. J. Lourens (2015), Obliquity forcing of low-latitude climate, *Clim. Past*, *11*, 1335–1346, doi:10.5194/cp-11-1335-2015.

Boulila, S., B. Galbrun, J. Laskar, and H. Pälike (2012), A ~9 Myr cycle in Cenozoic δ^{13}C record and long-term orbital eccentricity modulation: Is there a link?, *Earth Planet. Sci. Lett.*, *317*, 273–281, doi:10.1016/j.epsl.2011.11.017.

Broecker, W. S., and T.-H. Peng (1974), Gas exchange rates between air and sea, *Tellus*, *26*, 21–35.

Cheng, H., et al. (2016), The Asian monsoon over the past 640,000 years and ice age terminations, *Nature*, *534*, 640–646, doi:10.1038/nature18591.

Cramer, B. S., J. D. Wright, D. V. Kent, and M.-P. Aubry (2003), Orbital climate forcing of δ^{13}C excursions in the late Paleocene-early Eocene (chrons C24n-C25n), *Paleoceanography*, *18*, 1097, doi:10.1029/2003PA000909.

Crowley, T. J., K.-Y. Kim, J. G. Mengel, and D. A. Short (1992), Modeling 100,000-year climate fluctuations in pre-Pleistocene time series, *Science*, *255*, 705–707, doi:10.1126/science.255.5045.705.

Curry, W., N. Shackleton, C. Richter, J. Backman, F. Bassinet, T. Bickert, and E. Maddox (1995), Proceedings of the Ocean Drilling Program: Initial reports, *College station, TX (Ocean Drilling Program)*, *154*, 5–10, doi:10.2973/odp.proc.ir.154.1995.

Dickens, G. R. (2003), Rethinking the global carbon cycle with a large, dynamic and microbially mediated gas hydrate capacitor, *Earth Planet. Sci. Lett.*, *213*, 169–183.

Galbraith, E. D., E. Y. Kwon, D. Bianchi, M. P. Hain, and J. L. Sarmiento (2015), The impact of atmospheric pCO$_2$ on carbon isotope ratios of the atmosphere and ocean, *Global Biogeochem. Cycles*, *29*, 307–324, doi:10.1002/2014GB004929.

Galeotti, S., S. Krishnan, M. Pagani, L. Lanci, A. Gaudio, J. C. Zachos, S. Monechi, G. Morelli, and L. Lourens (2010), Orbital chronology of Early Eocene hyperthermals from the Contessa Road section, central Italy, *Earth Planet. Sci. Lett.*, *290*, 192–200, doi:10.1016/j.epsl.2009.12.021.

Ghil, M., et al. (2002), Advanced spectral methods for climatic time series, *Rev. Geophys.*, *40*, 3–1–3-41, doi:10.1029/2000RG000092.

Graves, C. E., W.-H. Lee, and G. R. North (1993), New parameterizations and sensitivities for simple climate models, *J. Geophys. Res.*, *98*, 5025–5036, doi:10.1029/92JD02666.

Hansen, J., M. Sato, and R. Ruedy (1997), Radiative forcing and climate response, *J. Geophys. Res.*, *102*, 6831–6864, doi:10.1029/96JD03436.

Hinnov, L. A. (2000), New perspectives on orbitally forced stratigraphy, *Ann. Rev. Earth Planet. Sci.*, *28*, 419–475, doi:10.1146/annurev.earth.28.1.419.

Holbourn, A., W. Kuhnt, M. Schulz, J.-A. Flores, and N. Andersen (2007), Orbitally-paced climate evolution during the middle Miocene "Monterey" carbon-isotope excursion, *Earth Planet. Sci. Lett.*, 534–550, doi:10.1016/j.epsl.2007.07.026.

Huybers, P., and C. Wunsch (2003), Rectification and precession signals in the climate system, *Geophys. Res. Lett.*, *30*, 2011, doi:10.1029/2003GL017875.

Imbrie, J., J. D. Hays, D. G. Martinson, A. McIntyre, A. C. Mix, J. J. Morley, N. G. Pisias, W. L. Prell, and N. J. Shackleton (1984), The orbital theory of Pleistocene climate: Support from a revised chronology of the marine δ^{18}O record, in *Milankovitch and Climate, Part 1*, pp. 269–305, D. Reidel, Dordrecht, Netherlands.

John, E. H., P. N. Pearson, H. K. Coxall, H. Birch, B. S. Wade, and G. L. Foster (2013), Warm ocean processes and carbon cycling in the Eocene, *Phil. Trans. R. Soc. A*, *317*, 20130099, doi:10.1098/rsta.2013.0099.

Jones, D. C., T. Ito, Y. Takano, and W.-C. Hsu (2014), Spatial and seasonal variability of the air-sea equilibration timescale of carbon dioxide, *Global Biogeochem. Cycles*, *28*, 1163–1178, doi:10.1002/2014GB004813.

Kallinger, T., P. Reegen, and W. W. Weiss (2008), A heuristic derivation of the uncertainty for frequency determination in time series data, *Astron. Astrophys.*, *481*, 571–574, doi:10.1051/0004-6361:20077559.

Kirtland Turner, S. (2014), Pliocene switch in orbital-scale carbon cycle/climate dynamics, *Paleoceanography*, *29*, 1256–1266, doi:10.1002/2014PA002651.

Komar, N., R. E. Zeebe, and G. R. Dickens (2013), Understanding long-term carbon cycle trends: The late Paleocene through the early Eocene, *Paleoceanography*, *28*, 650–662, doi:10.1002/palo.20060.

Konijnendijk, T. Y. M., S. L. Weber, E. Tuenter, and M. van Weele (2011), Methane variations on orbital timescales: A transient modeling experiment, *Clim. Past*, *7*, 635–648, doi:10.5194/cp-7-635-2011.

Kwon, E. Y., F. Primeau, and J. L. Sarmiento (2009), The impact of remineralization depth on the air-sea carbon balance, *Nat. Geosci.*, *2*, 630–635, doi:10.1038/ngeo612.

Laskar, J., P. Robutel, F. Joutel, M. Gastineau, A. C. M. Correia, and B. Levrard (2004), A long-term numerical solution for the insolation quantities of the Earth, *Astron. Astrophys.*, *428*, 261–285, doi:10.1051/0004–6361:20041335.

Laskar, J., A. Fienga, M. Gastineau, and H. Manche (2011), La2010: A new orbital solution for the long-term motion of the Earth, *Astron. Astrophys.*, *532*, A89, doi:10.1051/0004-6361/201116836.

Lauretano, V., F. Hilgen, J. Zachos, and L. Lourens (2016), Astronomically tuned age model for the early Eocene carbon isotope events: A new high-resolution δ^{13}C benthic record of ODP Site 1263 between ~49 and ~54 Ma, *Newslett. Stratigr.*, *49*, 383–400, doi:10.1127/nos/2016/0077.

Laurin, J., S. R. Meyers, D. Uličný, I. Jarvis, and B. B. Sageman (2015), Axial obliquity control on the greenhouse carbon budget through middle- to high-latitude reservoirs, *Paleoceanography*, *30*, 133–149, doi:10.1002/2014PA002736.

Lean, J., and D. Rind (2001), Earth's response to a variable Sun, *Science*, *292*, 234–236, doi:10.1126/science.1060082.

Littler, K., U. Röhl, T. Westerhold, and J. C. Zachos (2014), A high-resolution benthic stable-isotope record for the South Atlantic: Implications for orbital-scale changes in Late Paleocene-Early Eocene climate and carbon cycling, *Earth Planet. Sci. Lett.*, *401*, 18–30, doi:10.1016/j.epsl.2014.05.054.

Lourens, L. J., A. Sluijs, D. Kroon, J. C. Zachos, E. Thomas, U. Röhl, J. Bowles, and I. Raffi (2005), Astronomical pacing of late Palaeocene to early Eocene global warming events, *Nature*, *435*, 1083–1087, doi:10.1038/nature03814.

Ma, W., J. Tian, Q. Li, and P. Wang (2011), Simulation of long eccentricity (400-kyr) cycle in ocean carbon reservoir during Miocene Climate Optimum: Weathering and nutrient response to orbital change, *Geophys. Res. Lett.*, *38*, L10701, doi:10.1029/2011GL047680.

Mann, M. E., and J. M. Lees (1996), Robust estimation of background noise and signal detection in climatic time series, *Clim. Change*, *33*(3), 409–445, doi:10.1007/BF00142586.

Matsumoto, K. (2007), Biology-mediated temperature control on atmospheric pCO$_2$ and ocean biogeochemistry, *Geophys. Res. Lett.*, *34*, L20605, doi:10.1029/2007GL031301.

Meyers, S. R. (2012), Seeing red in cyclic stratigraphy: Spectral noise estimation for astrochronology, *Paleoceanography*, *27*, PA3228, doi:10.1029/2012PA002307.

Meyers, S. R. (2014), Astrochron: An R Package for Astrochronology. [Available at http://cran.r-project.org/ package=astrochron.]

Meyers, S. R. (2015), The evaluation of eccentricity-related amplitude modulation and bundling in paleoclimate data: An inverse approach for astrochronologic testing and time scale optimization, *Paleoceanography*, *30*, 1625–1640.

Montgomery, M. H., and D. O'Donoghue (1999), A derivation of the errors for least squares fitting to time series data, *Delta Scuti Star Newslett.*, *13*, 28–32.

Muller, R. A., and G. J. MacDonald (2002), *Ice Ages and Astronomical Causes: Data, Spectral Analysis and Mechanisms, Environmental Sciences*, 318 pp., Springer, Berlin.

Myhre, G., E. J. Highwood, K. P. Shine, and F. Stordal (1998), New estimates of radiative forcing due to well mixed greenhouse gases, *Geophys. Res. Lett.*, *25*, 2715–2718.

Pälike, H., J. Frazier, and J. C. Zachos (2006a), Extended orbitally forced palaeoclimatic records from the equatorial Atlantic Ceara Rise, *Quat. Sci. Rev.*, *25*, 3138–3149, doi:10.1016/j.quascirev.2006.02.011.

Pälike, H., R. D. Norris, J. O. Herrle, P. A. Wilson, H. K. Coxall, C. H. Lear, N. J. Shackleton, A. K. Tripati, and B. S. Wade (2006b), The heartbeat of the Oligocene climate system, *Science*, *314*, 1894–1898, doi:10.1126/science.1133822.

Park, J., S. L. D'Hondt, J. W. King, and C. Gibson (1993), Late Cretaceous precessional cycles in double time: A warm-Earth Milankovitch response, *Science*, *261*, 1431–1434, doi:10.1126/science.261.5127.1431.

Patterson, M. O., R. M. Mckay, T. Naish, C. Escutia, F. J. Jimenez-Espejo, M. E. Raymo, L. Tauxe, and H. Brinkhuis (2014), Orbital forcing of the East Antarctic ice sheet during the Pliocene and Early Pleistocene, *Nat. Geosci.*, *7*, 841–847, doi:10.1038/ngeo2273.

Percival, D., and A. Walden (1993), *Spectral Analysis for Physical Applications Multitaper and Conventional Univariate Techniques*, 583 pp., Cambridge Univ. Press, New York.

Ridgwell, A., and R. E. Zeebe (2005), The role of the global carbonate cycle in the regulation and evolution of the Earth system, *Earth Planet. Sci. Lett.*, *234*, 299–315.

Ripepe, M., and A. G. Fischer (1991), Stratigraphic rhythms synthesized from orbital variations, *Sediment. Model.*, *233*, 335–344.

Röhl, U., T. J. Bralower, R. D. Norris, and G. Wefer (2000), New chronology for the late Paleocene thermal maximum and its environmental implications, *Geology*, *28*, 927–930.

Russon, T., D. Paillard, and M. Elliot (2010), Potential origins of 400–500 kyr periodicities in the ocean carbon cycle: A box model approach, *Global Biogeochem. Cycles*, *24*, GB2013, doi:10.1029/2009GB003586.

Shackleton, N. J., S. J. Crowhurst, G. P. Weedon, and J. Laskar (1999), Astronomical calibration of Oligocene-Miocene time, *Phil. Trans. R. Soc. A*, *357*, 1907–1929, doi:10.1098/rsta.1999.0407.

Short, D. A., J. G. Mengel, T. J. Crowley, W. T. Hyde, and G. R. North (1991), Filtering of Milankovitch cycles by Earth's geography, *Quat. Res.*, *35*, 157–173, doi:10.1016/0033-5894(91)90064-C.

Thomson, D. J. (1982), Spectrum estimation and harmonic analysis, *IEEE Proc.*, *70*, 1055–1096.

Tung, K. K., J. Zhou, and C. D. Camp (2008), Constraining model transient climate response using independent observations of solar-cycle forcing and response, *Geophys. Res. Lett.*, *35*, L17707, doi:10.1029/2008GL034240.

Uchikawa, J., and R. E. Zeebe (2008), Influence of terrestrial weathering on ocean acidification and the next glacial inception, *Geophys. Res. Lett.*, *35*, L23608, doi:10.1029/2008GL035963.

van Dam, J. A., H. Abdul Aziz, M. Ángeles, F. J. Álvarez Sierra, L. W. Hilgen, O. van den Hoek, L. J. Lourens, P. Mein, A. J. van der Meulen, and P. Pelaez-Campomanes (2006), Long-period astronomical forcing of mammal turnover, *Nature*, *443*, 687–691, doi:10.1038/nature05163.

Vaughan, S., R. J. Bailey, and D. G. Smith (2014), Cyclostratigraphy: Data filtering as a source of spurious spectral peaks, *Geol. Soc. London, Spec. Publ.*, *404*, 151–156, doi:10.1144/SP404.11.

Verschuren, D., J. S. Sinninghe Damsté, J. Moernaut, I. Kristen, M. Blaauw, M. Fagot, and G. H. Haug (2009), CHALLACEA project members: Half-precessional dynamics of monsoon rainfall near the East African Equator, *Nature*, *462*, 637–641, doi:10.1038/nature08520.

Wang, P., J. Tian, and L. J. Lourens (2010), Obscuring of long eccentricity cyclicity in Pleistocene oceanic carbon isotope records, *Earth Planet. Sci. Lett.*, *290*, 319–330, doi:10.1016/j.epsl.2009.12.028.

Wang, P., Q. Li, J. Tian, Z. Jian, C. Liu, L. Li, and W. Ma (2014), Long-term cycles in the carbon reservoir of the Quaternary ocean: A perspective from the South China Sea, *Nat. Sci. Rev. Chin. Acad. Sci.*, *1*(1), 119–143.

Westerhold, T., and U. Röhl (2013), Orbital pacing of Eocene climate during the middle Eocene climate optimum and the chron C19r event: Missing link found in the tropical western Atlantic, *Geochem. Geophys. Geosys.*, *14*, 4811–4825, doi:10.1002/ggge.20293.

Westerhold, T., U. Röhl, J. Laskar, I. Raffi, J. Bowles, L. J. Lourens, and J. C. Zachos (2007), On the duration of magnetochrons C24r and C25n and the timing of early Eocene global warming events: Implications from the Ocean Drilling Program Leg 208 Walvis Ridge depth transect, *Paleoceanography*, *22*, PA2201, doi:10.1029/2006PA001322.

Westerhold, T., U. Röhl, I. Raffi, E. Fornaciari, S. Monechi, V. Reale, J. Bowles, and H. F. Evans (2008), Astronomical calibration of the Paleocene time, *Palaeogeogr. Palaeoclim. Palaeoecol.*, *257*(4), 377–403.

Westerhold, T., U. Röhl, B. Donner, H. K.McCarren, and J. C. Zachos (2011), A complete high-resolution Paleocene benthic stable isotope record for the central Pacific (ODP Site 1209), *Paleoceanography*, *26*, PA2216, doi:10.1029/2010PA002092.

Westerhold, T., U. Röhl, T. Frederichs, S. M. Bohaty, and J. C. Zachos (2015), Astronomical calibration of the geological timescale: Closing the middle Eocene gap, *Clim. Past*, *11*(9), 1181–1195, doi:10.5194/cp-11-1181-2015.

Zachos, J. C., M. Pagani, L. Sloan, E. Thomas, and K. Billups (2001a), Trends, rhythms, and aberrations in global climate 65 Ma to present, *Science*, *292*, 686–693.

Zachos, J. C., N. J. Shackleton, J. S. Revenaugh, H. Pälike, and B. P. Flower (2001b), Climate response to orbital forcing across the Oligocene-Miocene boundary, *Science*, *292*, 274–278, doi:10.1126/science.1058288.

Zachos, J. C., et al. (2005), Rapid acidification of the ocean during the Paleocene-Eocene Thermal Maximum, *Science*, *308*, 1611–1615.

Zachos, J. C., H. McCarren, B. Murphy, U. Röhl, and T. Westerhold (2010), Tempo and scale of late Paleocene and early Eocene carbon isotope cycles: Implications for the origin of hyperthermals, *Earth Planet. Sci. Lett.*, *299*, 242–249, doi:10.1016/j.epsl.2010.09.004.

Zeebe, R. E. (2012), LOSCAR: Long-term Ocean-atmosphere-Sediment CArbon cycle Reservoir Model v2.0.4, *Geosci. Model Dev.*, *5*, 149–166.

Zeebe, R. E. (2013a), What caused the long duration of the Paleocene-Eocene Thermal Maximum?, *Paleoceanography*, *28*, 440–452, doi:10.1002/palo.20039.

Zeebe, R. E. (2013b), Time-dependent climate sensitivity and the legacy of anthropogenic greenhouse gas emissions, *Proc. Nat. Acad. Sci.*, *110*, 13,739–13,744, doi:10.1073/pnas.1222843110.

Zeeden, C., S. R. Meyers, L. J. Lourens, and F. J. Hilgen (2015), Testing astronomically tuned age models, *Paleoceanography*, *30*, 369–383, doi:10.1002/2014PA002762.